Nonlinear Dyn
https://doi.org/10.1007/s11071-025-11668-1

RESEARCH

Spectral submanifold reduction of high dimensional nonlinear systems for dynamical integrity analysis

Giuseppe Habib · Mattia Cenedese · Giuseppe Rega

Received: 25 December 2024 / Accepted: 27 July 2025

Abstract This study leverages spectral submanifold (SSM) theory for model-order reduction to investigate the dynamical integrity of complex engineering systems, specifically, a finite element model of a clamped-clamped von Kármán beam, an experimental water tank with liquid sloshing, a numerical model of a forced pitch-and-plunge airfoil subject to flutter instability, and an axially compressed beam undergoing dynamic buckling. The main objective of this research is to establish an efficient approach for evaluating the dynamical integrity of high-dimensional and experimental systems by exploiting SSM-model reduction techniques. In each case, SSM-based reduced order models are constructed directly from time-series data, leading to reduced systems of minimal dimensionality (2 or 3) that fully capture the most relevant global dynamical phenomena from a qualitative and quantitative viewpoint. This reduction enables the computation of standard dynamical integrity measures with a fraction of the computational cost required by traditional methods. The approach not only validates SSM theory for global dynamics analysis but also highlights its potential as a practical tool for integrating dynamical integrity assessments into engineering design—a step often overlooked in standard practice.

Keywords Spectral submanifold · Dynamical integrity · Reduced order model · Data driven

G. Habib
Department of Applied Mechanics, Faculty of Mechanical Engineering, Budapest University of Technology and Economics, Műegyetem rkp. 3., Budapest 1111, Hungary

G. Habib (✉)
MTA-BME Lendület "Momentum" Global Dynamics Research Group, Műegyetem rkp. 3., Budapest 1111, Hungary
e-mail: habib@mm.bme.hu

M. Cenedese
Institute for Mechanical Systems, ETH Zürich, Leonhardstrasse 21, 8092 Zürich, Switzerland

G. Rega
Department of Structural and Geotechnical Engineering, Sapienza – University of Rome, Via A. Gramsci, 53, 00197 Rome, Italy

1 Introduction

In engineering practice, stability analysis is a fundamental step that often distinguishes between acceptable and unacceptable designs for dynamical systems. However, this is not sufficient for nonlinear systems. Indeed, it is common that although a dynamical steady state is stable, its dynamical integrity is limited, meaning that sufficiently large perturbations might make the system leave the basin of attraction (BoA) of the solution of interest, leading it to other potentially dangerous trajectories. This phenomenon is encountered in many systems of practical interest, such as machine tool vibrations [1,2], aerodynamic flutter [3,4], shear flows [5], particle escape [6,7], ship capsizing [8], shimmy instability [9,10], dynamic vibration absorbers [11,12], impact oscillators [13], human balance [14],

Published online: 25 August 2025

valve dynamics [15], robot control [16], power grids [17], to name a few.

The full knowledge of the BoA enables one to characterize the dynamical integrity of a steady-state solution. However, there are two major problems related to this operation: quantifying the dynamical integrity from the BoA and identifying the BoA itself. The former issue was solved by the introduction of several dynamical integrity measures [18,19], such as the global integrity measure (GIM), the local integrity measure (LIM), the impulsive integrity measure, the stochastic integrity measure, the integrity factor (IF) and the actual global integrity measure [20,21]. Although each dynamical integrity measure is different from the others, they all aim at quantifying the dynamical integrity of a steady-state solution. Therefore, they enable the study of the trend of the dynamical integrity with respect to parameter variations, an important aspect for implementing dynamical integrity analysis in engineering practice.

Several methods exist for the identification of a solution's BoA, which is typically done numerically. The most intuitive numerical method consists of performing many numerical simulations of the system with different initial conditions. This approach enables obtaining two-dimensional sections of a BoA but can hardly be implemented on larger dimensional systems. Additionally, it is inherently inefficient, as it uses only one bit of information from each trajectory. The arguably most efficient numerical method is the cell-mapping method, developed by Hsu in 1980 [22–24], which exploits a discretization in cells of the phase space, short numerical simulations starting from each cell, and Markov chains [25,26] for the definition of steady-state solutions and their BoAs. Although the method is computationally very efficient and easily parallelizable, it presents memory issues for large-dimensional dynamical systems, which limits its implementation [27]. Other numerical methods to quantify the dynamical integrity exploit probabilistic approaches based on Monte Carlo sampling [28,29]; although some of them are computationally efficient, their outcome is not comparable with classical integrity measures and they fail to provide a meaningful insight into the dynamics of the system.

Analytical methods are typically based on Lyapunov functions [5,30,31]; however, their computation is often challenging, and there is no general procedure to do it. Besides, they provide an underestimate of a BoA, which is often excessively conservative. Attempts to compute a solution's BoA experimentally are relatively rare, mostly because of the difficulties in imposing specific initial conditions. The few studies on the topic include the works by Virgin and co-authors [32,33] about non-smooth oscillators and the ones from Zakynthinaki and co-authors [34] related to human balancing. Recently, a numerical method to estimate the LIM without requiring computing the BoA was developed [35] and extended to time-delayed systems [36]. Although the method is effective because it bypasses the computation of the BoA, it has significant limitations for large-dimensional systems.

Although each method for dynamical integrity computation presents its own limitations, they all suffer the so-called curse of dimensionality [37], which means that memory requirements and computational time grow exponentially with the system dimension [38]. This phenomenon makes the direct computation of the dynamical integrity of large dynamical systems practically impossible. Even for medium-size systems, dynamical integrity computation is usually excessively time-consuming, hindering its use for engineering design.

A possible solution for this problem is to reduce the system dimension through a model reduction technique, as also discussed in a recent overview on nonlinear dynamics in mechanics [39]. Several strategies for this purpose exist. Methods based on invariant manifolds exploit the center manifold reduction [40,41], nonlinear normal modes [42,43], or spectral submanifolds (SSMs) [44]. Other approaches include normal form methods [45,46], direct perturbation techniques [47], the rectified Galerkin method [48] and the recently developed low order elimination technique [49,50].

Each technique presents its advantages and limitations; however, the SSM theory seems particularly fit for dynamical integrity analysis of large dynamical systems because it can be rapidly carried out either from equations of motion [44,51] or from only trajectory data [52–54], which is particularly appealing for its implementation to unmodelled real systems or high-dimensional models, potentially coming from commercial finite element (FE) codes as also discussed in [55]. Applications of data-driven SSMs also include fluid dynamics [56,57], non-smooth mechanical systems [58] and controls [59], also using videos as inputs to the algorithms extracting the SSM [60].

In this study, we exploit SSM theory, and in particular the `SSMLearn` toolbox, to study the dynamical integrity and test it on various systems. The objective of the study is twofold. On the one hand, it illustrates that the SSM model reduction is accurate not only in describing a system's steady-state solutions but also regarding its global dynamics. On the other hand, it illustrates how this model reduction technique produces models for which the dynamical integrity analysis becomes very easy but still accurate. The proposed method is applied to four qualitatively different systems: an FE model of a clamped-clamped von Kármán beam, an experimental setup of water sloshing in a tank, a reduced model of an airfoil undergoing flutter instability, and an FE model of an axially compressed beam undergoing dynamic buckling.

2 Methods

2.1 Data-driven spectral submanifolds

The SSMs are the unique, smoothest invariant submanifolds that act as nonlinear continuations of stable or unstable spectral subspaces of an equilibrium under the addition of nonlinearity to the system linearization [44]. In general, SSMs are also defined for non-autonomous attractors, which enables them to be used for studying systems with external forcing. More recently, secondary (or fractional) SSMs, as well as SSMs with mixed stability, have been studied [61]. SSMs can be extracted from the system equations of motion [51] as well as from data using a few trajectories [52]. For purposes of model reduction, slow SSMs are the most relevant candidate for model reduction [52], which are normally hyperbolic and hence robust under perturbations. Here, trajectories synchronize exponentially fast to these manifolds, which are, compared to other projection-based model reduction methods, exact sets of solutions of the nonlinear dynamical systems capturing the dominant dynamics. More broadly, slow SSMs form a nested structure of attractors, allowing for the construction of a hierarchy of reduced-order models (ROMs) where trajectories converge at an exponential rate. In addition, it has been shown that data-driven autonomous SSMs can be used to predict forced motions as well as feedback-controlled motions [52,59]. Therefore, SSMs are configured as promising candidates for studying the system's dynamical integrity, and we exploit their data-driven extraction in this paper.

To learn SSMs from data, we leverage the algorithm `SSMLearn` [52], which has the following key steps. First, trajectories are generated (either via numerical simulations or physical experiments) sufficiently close to the target SSM. In the case of stable SSMs, a successful strategy is to initialize them from near-resonant conditions and let the system decay to an equilibrium point through free vibrations [53]. Second, the measurement needs to be appropriately embedded. Depending on the available observables and the size of the target SSM, the algorithm retrieves a space where the SSM can be embedded with probability one either via Whitney or Takens embedding theorems, where, in the latter, delay-embedding is exploited; see also [62] for additional details. Then, a Taylor expansion of the d-dimensional SSM is learned from data. Specifically, a mean-square error minimization procedure is exploited to identify the coefficients of polynomial models truncated to a certain degree both for the geometry and the reduced dynamics. As a last step, the SSM dynamics is further reduced to an extended normal form, analogous to Poincaré normal forms usually implemented in bifurcation theory. This normal form is particularly useful as it enables to directly extract backbone curves, damping curves, and forced response curves [55] upon adding periodic or quasi-periodic forcing to the system autonomous dynamics learned from data.

2.2 Dynamical integrity measures

As discussed in Sect. 1, dynamical integrity measures are scalar quantities utilized to quantify the dynamical integrity of a steady-state solution. Several dynamical integrity measures exist, as thoroughly explained in [38], and each of them can quantify the dynamical integrity from a slightly different perspective, generally concerning the extent and shape of the BoA.

In this study, we consider the GIM, the IF, and the LIM. The GIM is defined as the portion of space occupied by the BoA of a solution with respect to the whole portion of phase space considered. It is probably the most intuitive way to quantify the dynamical integrity of a solution, and it is easy to compute once the BoA is identified. Its main limitation is that it also includes intermingled and fractal portions of the BoA, which

usually are not of practical interest, especially if leaving the BoA can have critical consequences.

The IF was developed specifically to overcome this limitation. It is defined as the radius of the largest hypersphere entirely included in the BoA of a solution. As such, it automatically rules out all intermingled and fractal regions and provides a measure of the most compact region of the BoA. Accordingly, it provides a quantity typically more significant from an engineering perspective. Its calculation is not trivial. In fact, not only is the dimension of the largest hypersphere unknown, but its position is also unknown. Another problem of the IF is that the phase space is generally non-isotropic; therefore, the various directions should be normalized to define a hypersphere. Possible solutions to this problem are proposed in [35].

The LIM is similar in scope and practical significance to the IF. It is defined as the largest hypersphere entirely included in the BoA of a solution, centered at the solution. Because of this additional constraint, the LIM is never larger than the IF and can be computed much more easily. In fact, it corresponds to the minimal distance between the solution and any point of the phase space not included in the BoA. In the case of solutions different from equilibrium points, it can be defined as the minimal distance between any point of the solution and any point of the phase space not included in the BoA [63].

As illustrated below, the first three systems considered in this study have ROMs of sufficiently small dimension that the BoA can be easily computed. Accordingly, the identification of the integrity measures is not particularly complicated and computationally inexpensive. For the last investigated system (Sect. 3.4), the LIM is computed through the `DynIn` toolbox [35,36,63], which can rapidly provide the LIM bypassing the computation of the BoA. This example further illustrates how the SSM model reduction can be effectively coupled with DI assessment algorithms.

3 Examples

The procedure is applied to four different systems: the FE model of a forced clamped-clamped von Kármán beam, liquid sloshing in a water tank, a numerical model of a forced pitch-and-plunge airfoil undergoing flutter instability, and the FE model of an axially compressed von Kármán beam undergoing dynamic buckling.

3.1 Clamped-clamped von Kármán beam

As a first example, we analyze an FE model of a von Kármán beam [64] with clamped-clamped boundary conditions, as depicted in Fig. 1a . The ROM derivation follows the same model and methodology as in [52,55], while the novelty of this study lies in the dynamical integrity analysis of the ROM. This beam model accounts for moderate deformations by incorporating a quadratic term in the kinematic formulation. The structure is discretized into 12 elements, employing cubic shape functions for the transverse deflection and linear shape functions for the axial displacement. The obtained model comprises 33 degrees of freedom (DOFs) and represents an aluminum beam with dimensions of length 1 [m], width 5 [cm], and thickness 2 [cm], with a material damping modulus of 10^6 [Pa-sec], Young's modulus of 70 [GPa], density of 2700 [kg/m^3], and Poisson ratio of 0.3. The slowest eigenvalue is approximately $-3.09 + \mathrm{i}657.72$.

The ratio between the real parts of the second and first slowest modes is 7.6. This indicates that the decay along the second or higher modes is over seven times faster than along the first mode. Consequently, our objective is to construct a reduced-order model (ROM) for this beam utilizing the slowest two-dimensional SSM, which corresponds to the nonlinear continuation of the first mode of vibration.

To collect data near the SSM, we employed initial conditions based on static loading, as discussed in Sect. 2.1. In particular, we applied a force f at the midpoint of the beam and measured the transverse displacement q_B at this point, as illustrated in Fig. 1a . This forcing method produces a static displacement similar to the first mode shape. Consequently, an unforced trajectory starting from such a displacement is expected to rapidly converge to the SSM. For training and testing, we selected initial amplitudes corresponding to a displacement q_B of approximately 2 [mm]. Subsequently, we trained a seventh-order model using `SSMLearn`, from which the reduced dynamics are obtained as follows:

$$\dot{\rho} = \alpha(\rho)\,\rho = -3.09\rho - 1.5981\rho^3 + 2.5781\rho^5 + 0.78938\rho^7$$

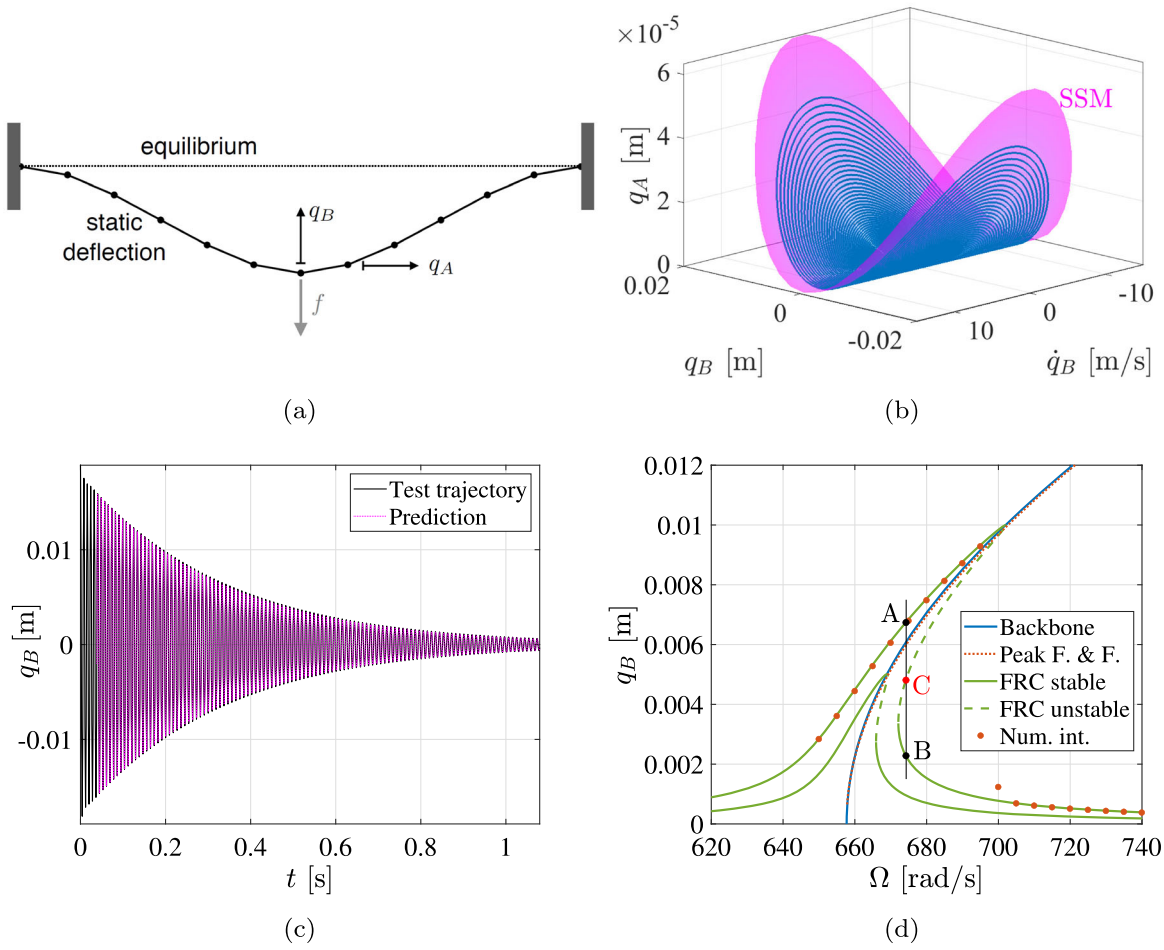

Fig. 1 **a** FE discretization of the clamped-clamped beam model. **b** SSM in the physical space (magenta) along with the training trajectory (blue). **c** Test trajectory from a numerical simulation of the full model (black) and its prediction (magenta) from the `SSMLearn` ROM. **d** Frequency response curve for forcing values $f = 0.4872$ [N] and 1.026 [N], and backbone computed from the `SSMLearn` ROM, compared with results from numerical integration; labels A, B and C refer to the steady-state solutions represented in Fig. 2a. Color figure online

$$\dot{\theta} = \omega(\rho) = 657.7165 + 469.4588\rho^2 - 308.6857\rho^4 - 103.9901\rho^6. \quad (1)$$

The ROM has a dimension of 2, which provides significant computational advantages compared to the original system of dimension 66. ρ is related to the amplitude of oscillation, while θ to the phase.

The ROM also captures the SSM geometry, illustrated in Fig. 1b with the training trajectory. The figure is in the coordinates q_B, $\dot{q}_B$ and q_A, where the axial displacement q_A of the midpoint is shown as a function of its bending displacement q_B and velocity $\dot{q}_B$. This representation highlights how the SSM geometry encapsulates the nonlinear coupling between bending and stretching in the beam. This ROM provides a normalized mean-trajectory-error of 3.597 % for the test trajectory; test and predicted trajectories are compared in Fig. 1c . Additionally, the ROM generates the instantaneous frequency backbone curve (blue line in Fig. 1d). The x-axis of the backbone curve represents the oscillation frequency; its intersection with the zero amplitude marks the linearized natural frequency. We note that the instantaneous frequency backbone closely aligns with the frequencies directly extracted from the

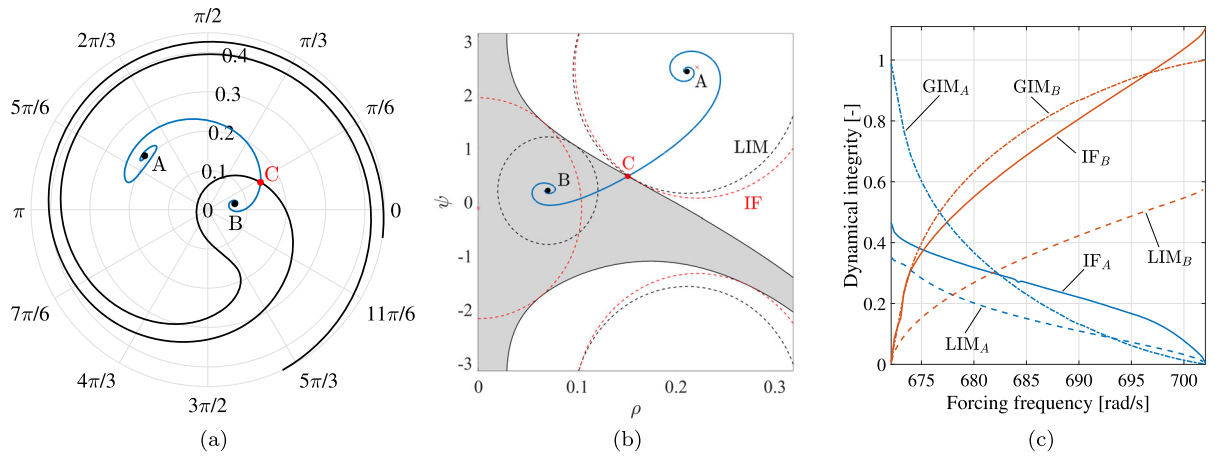

Fig. 2 **a** Phase portrait in the ψ, ρ space in polar coordinates for $\Omega = 674.3$ [rad/s] and $f = 1.026$ [N]; A, B and C mark the two stable and the unstable equilibria, respectively; black lines depict BoA boundaries, while blue lines trajectories from the unstable to the stable equilibria. **b** Phase portrait in the ψ, ρ space in Cartesian coordinates; the red circles indicate the IF and the black ones the LIM. **c** Trends of the IF, LIM, and GIM of equilibria A and B for varying forcing frequency

training trajectory (dotted red curve in Fig. 1d) using the Peak Finding and Fitting signal processing method [65].

Next, we analyze the system's forced response utilizing the SSM-based ROM in normal form. To introduce periodic forcing, we modify the static force applied at the midpoint into a time-periodic one. This step leads to the system of equation

$$\begin{aligned} \dot{\rho} &= \alpha(\rho)\rho + f\sin(\psi) \\ \dot{\psi} &= \omega(\rho) - \Omega + \frac{f}{\rho}\cos(\psi), \end{aligned} \tag{2}$$

where we introduced the phase shift $\psi = \theta - \Omega t$. More details on the procedure can be found in [52].

Equation (2) is an autonomous, planar, extended normal form of the system near resonance. Periodic solutions of the original system, either stable or unstable, are reduced to fixed points for the system (2). Their amplitudes ρ_0 and phases ψ_0 satisfy the equations

$$\begin{aligned} \Omega &= \omega(\rho_0) \pm \sqrt{\frac{f^2}{\rho_0^2} - \alpha^2(\rho_0)}, \\ \psi_0 &= \tan^{-1}\left(\frac{\alpha(\rho_0)}{\omega(\rho_0) - \Omega}\right). \end{aligned} \tag{3}$$

Through Eq. (3), the frequency response curve (FRC) can be directly obtained, as illustrated in Fig. 1d for $f = 0.4872$ and 1.026 [N]. Red dots in Fig. 1d refer to numerical integrations of the full FE model, exhibiting an excellent agreement with the FRC provided by the SSM-based ROM.

The system presents a classical hardening behavior, leading to a resonant peak bent to the right. Consequently, for a range of excitation frequency values near resonance, it presents two coexisting stable steady-state solutions and an unstable one (of saddle type). This is illustrated in the phase portrait in polar coordinates depicted in Fig. 2a, where the two stable solutions are marked with A and B. In the figure, the angular axis depicts ψ, while the radial axis marks ρ.

Since the system is only 2-dimensional, the BoA of the two stable solutions can be rapidly identified. In particular, the stable manifolds of the unstable solution correspond to the boundary of the two BoA. They can be obtained through a time-inverted numerical simulation of the system dynamics starting in the vicinity of the unstable solution. The full knowledge of the BoA makes the computation of dynamical integrity trivial. Although the polar representation provides an intuitive understanding of the system's dynamics, to compute the system's dynamical integrity, it is convenient to implement a Cartesian representation of the phase space, provided in Fig. 2b. The IF, the LIM, and the GIM are computed for both stable solutions. The IF is marked by the radius of the red circles, while the

LIM by the radius of the black circles. The GIM is given by the percentage of the area of each BoA with respect to the total considered area of the phase space. For this purpose, ψ is limited between $-\pi$ and π, while ρ between 0 and $\rho_{\max} = 0.318$, where $\rho_{\max}$ is chosen as the largest amplitude for which the ROM is trusted. During the computation, we did not require that the whole circle marking either the LIM or the IF be fully within the relevant portion of the phase space; only the center of the IF circle is constrained in this sense. The IF was computed by exploiting a genetic algorithm to identify the center of the largest circle in the BoA.

The trend of the dynamical integrity measures for the whole range of bistability is illustrated in Fig. 2c. All integrity measures are reduced to zero for the lower amplitude solution B on the left boundary of the frequency range, where the solution disappears, merging with the unstable solution through a saddle-node bifurcation. The same occurs for the higher amplitude solution A on the right frequency boundary. In general terms, it has to be noted that the two sets of dynamical integrity curves represent frequency-dependent profiles of robustness of the two solutions with respect to (possibly finite) variations of initial conditions. The corresponding BoAs are substantially compact and compete with each other within the frequency range of coexistence of the two solutions, as also reflected in the overall complementary trend of the corresponding curves. Although these trends are similar for the three measures, the frequency value for which the two solutions have the same dynamical integrity is slightly different in the three cases. As regards the integrity values obtained with the three measures, the LIM profile is always the lower one (though to a different extent for the two solutions), which is an outcome ensuing from its definition and already observed in the dynamical integrity evaluation of a large variety of systems [66]. The GIM profile is not always much higher than the other two profiles (as it often occurs because of also accounting for the fractal, i.e. unsafe, parts of the basin), because the BoAs of the two solutions in the frequency range of coexistence are essentially compact, as already mentioned.

In order to highlight the significance of the result, we also compare the frequency response and the computed dynamical integrity measures if the system dimension is reduced via a classical proper orthogonal decomposition (POD). The most significant difference is that the POD leads to a system possessing a significantly larger bistable region. For $f = 1.026$ [N], the SSM reduced system has coexisting stable solutions for $\Omega \in (672,\ 702)$ [rad/s]; while utilizing a POD the range of bistable behavior exists for $\Omega \in (674,\ 729)$ [rad/s], i.e., it is more than 80 % larger (Fig. 3a). Additionally, the POD-reduced system significantly underestimates the oscillation amplitude of the upper branch, as highlighted by the comparison with direct numerical integration of the full system (red dots in Fig. 3a).

The trend of the dynamical integrity measures for the POD-reduced system is illustrated in Fig. 3b. The overestimated extent of the bistable region necessarily leads to errors in the dynamical integrity. In fact, for $\Omega > 702$ [rad/s], solution B should be globally stable, and solution A not exist. Apart from this, we note that the POD-reduced system significantly overestimates the LIM of solution A, while the IF of solution B is underestimated. Additionally, we observe that the LIM is much closer to the IF in the case of the POD rather than for the SSM reduction. Nevertheless, the overall trend of the dynamical integrity is similar in the two cases.

The comparison of the dynamical integrity between the SSM-based ROM and the POD does not assess the overall accuracy of the global dynamics of the SSM-based ROM, which is computationally too expensive to be compared with the full system. However, it illustrates the relevance of the chosen system reduction technique concerning global dynamics.

3.2 Sloshing water in tank

As a second example, we examine fluid oscillations in a tank, which display highly softening behavior [67]. To capture the nonlinear effects observed in sloshing surface waves, Duffing-type models have been adopted in the literature [68]. Although these models well-approximate amplitude variations of forced experiments, identifying nonlinear damping remains a challenging task [69].

We consider sloshing experiments in a rectangular tank measuring 500 [mm] in width and 50 [mm] in depth, filled with water to a height of 400 [mm], as illustrated in Fig. 4a [52]. The tank was assembled on a platform driven by a motor with harmonic excitation. The water surface level was tracked through image processing techniques at a sampling time of $\Delta t = 0.033$ [s]. The horizontal position of the computed center of

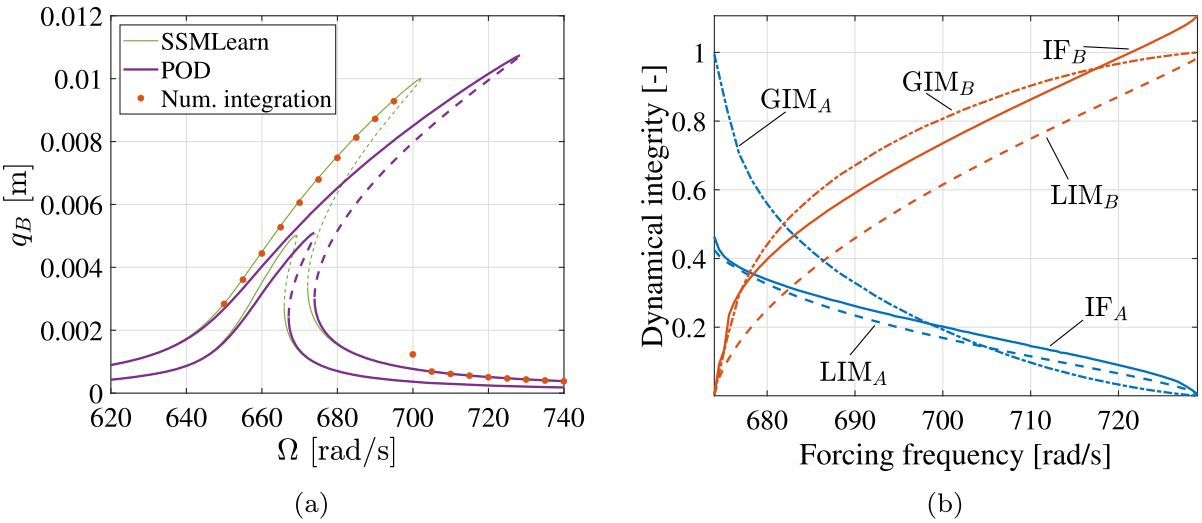

Fig. 3 **a** Frequency response curves. **b** Trends of the IF, LIM, and GIM of equilibria A and B for varying forcing frequency for the POD reduced system

mass of the water, normalized with respect to the tank width, was used as observable $s(t)$. This scalar quantity is both physically meaningful and robust against image processing errors [69]. In this study, we utilize the experimental data obtained in [52].

The system's unforced nonlinear dynamics is characterized using data from resonance decay experiments [70]. For free decay experiments, a shaker was implemented instead of a motor. In these experiments, the tank undergoes periodic horizontal displacement near resonance until a steady-state oscillation is established. At that point, the shaker is switched off, and the subsequent decay of the sloshing motion is recorded. Figure 4b (black line) illustrates an example of a decaying trajectory, with the shaker deactivated just before time zero. By design, this damped oscillation closely follows the system's slowest two-dimensional SSM. We use two of these decaying trajectories for training and one for validation to develop a two-dimensional ($d = 2$) autonomous SSM-based ROM for $s(t)$. The delay embedding dimension is set to $p = 5$, the minimal value required to be generically correct for embedding the SSM according to Takens's theorem [71]. Given this input and a maximaum reconstruction error of 2 %, `SSMLearn` provides a nearly flat SSM in the delayed observable space, represented by the cubic extended normal form

$$\begin{aligned}\dot{\rho} &= \alpha(\rho)\,\rho = -0.060676\rho - 0.046832\rho^3 \\ \dot{\theta} &= \omega(\rho) = 7.8131 - 1.3347\rho^2.\end{aligned} \tag{4}$$

The SSM is depicted in Fig. 4c (in magenta), along with a measured trajectory (blue curve). We remark that eventual differences in the coefficients of the reduced dynamics with that appearing in [52] are due to numerics only, as the same experimental data and procedure were used, but do not affect the accuracy and the dynamics behavior of the reduced-order model. This Stuart–Landau-type normal form, representing the lowest-order approximation for Andronov-Hopf bifurcations [72–74], serves as a highly accurate ROM, achieving a normalized mean trajectory error of just 1.88 % on the test dataset, as shown in Fig. 4b. The model captures the amplitude-dependent nonlinear damping, $\alpha(\rho)$, which is visualized in Fig. 4d as a function of the physical amplitude.

A separate series of experiments, using the setup depicted in Fig. 4a, focused on measuring the steady-state response of periodically forced sloshing during frequency sweeps. These tests were conducted at three distinct forcing displacement amplitudes, namely 0.09 %, 0.17 % and 0.32 % of the horizontal tank width. Similar to the approach taken in the beam example, we determine the corresponding forcing amplitude f at the peak response of each frequency sweep. The forced ROM reads:

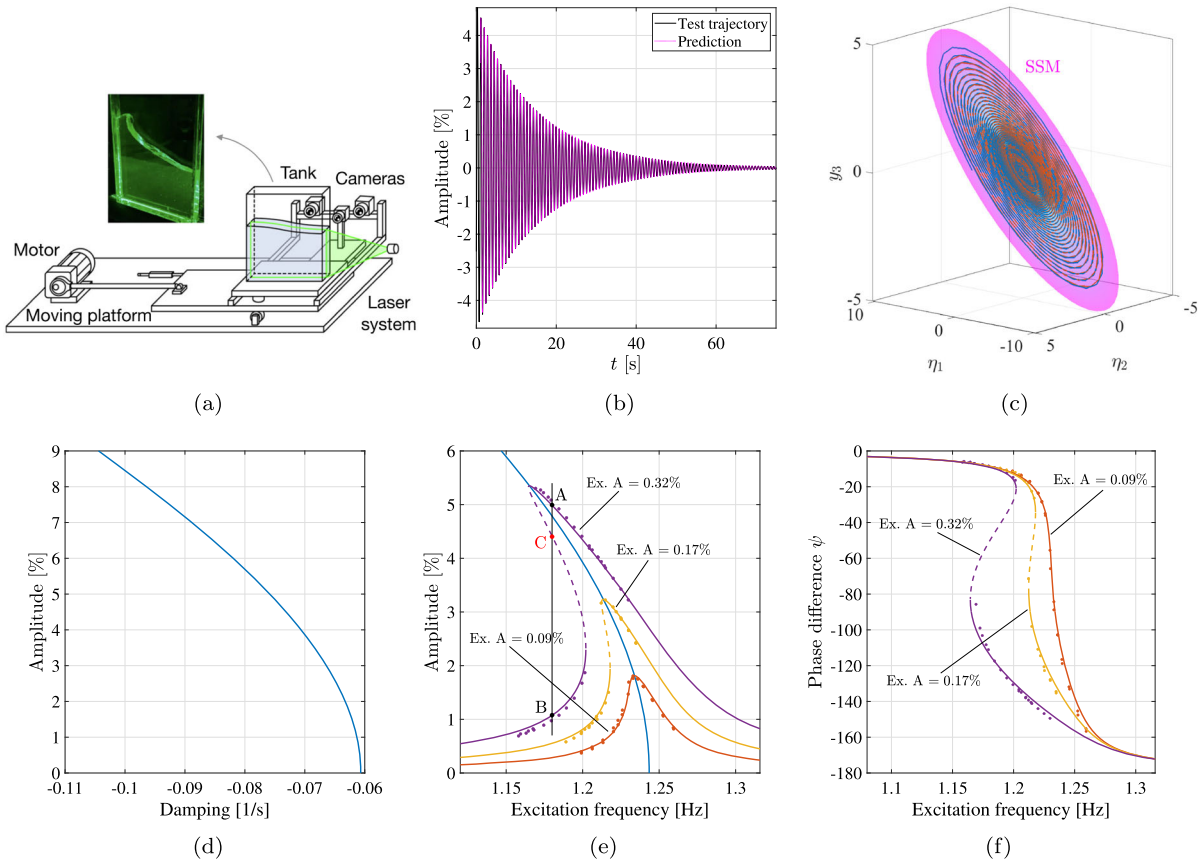

Fig. 4 **a** Schematic representation of the sloshing water experiment. **b** Test trajectory from experiments (black) and its prediction (magenta) from the `SSMLearn` ROM. **c** SSM in the physical space (magenta) along with the training trajectory (blue). **d** Damping backbone curve from the `SSMLearn` ROM. **e** Frequency response curve and backbone computed from the `SSMLearn` ROM; dots indicate measured frequency response amplitudes; A, B, and C letters refer to the steady-state solutions investigated in Fig. 5a . **f** Phase difference as a function of the excitation frequency computed from the `SSMLearn` ROM; dots indicate measured phase differences

$$\begin{aligned}\dot{\rho} &= -0.060676\rho - 0.046832\rho^3 + f\sin(\psi)\\ \dot{\psi} &= 7.8131 - 1.3347\rho^2 - \Omega + \frac{f}{\rho}\cos(\psi)\,;\end{aligned} \tag{5}$$

where $\psi = \theta - \Omega t$, as in the beam example.

Figure 4e depicts the FRC obtained in closed form using Eq. (3). The solid lines, corresponding to the ROM prediction, closely match the dots obtained experimentally. The phase ψ of the forced response relative to the forcing has been found difficult to fit to forced Duffing-type models [69], but the present modeling methodology also predicts this phase accurately using the second expression in Eq. (3), as illustrated in Fig. 4f.

Next, we study the dynamical integrity of the system's coexisting stable periodic solutions, exploiting the ROM. Computing such analysis experimentally would be extremely complicated, as illustrated by previous attempts to compute dynamical integrity and BoA experimentally [32,34,75]. The planar dimension of the ROM greatly facilitates the computation of the BoA and of the dynamical integrity. The mathematical formulation of the ROM has the same shape as the beam example; therefore, the same procedure is applied. The BoA boundaries correspond to the stable manifolds of the unstable periodic solution (fixed point for the ROM), which can be directly computed through time-inverted numerical integration starting in the vicinity of the unstable solution. The boundaries

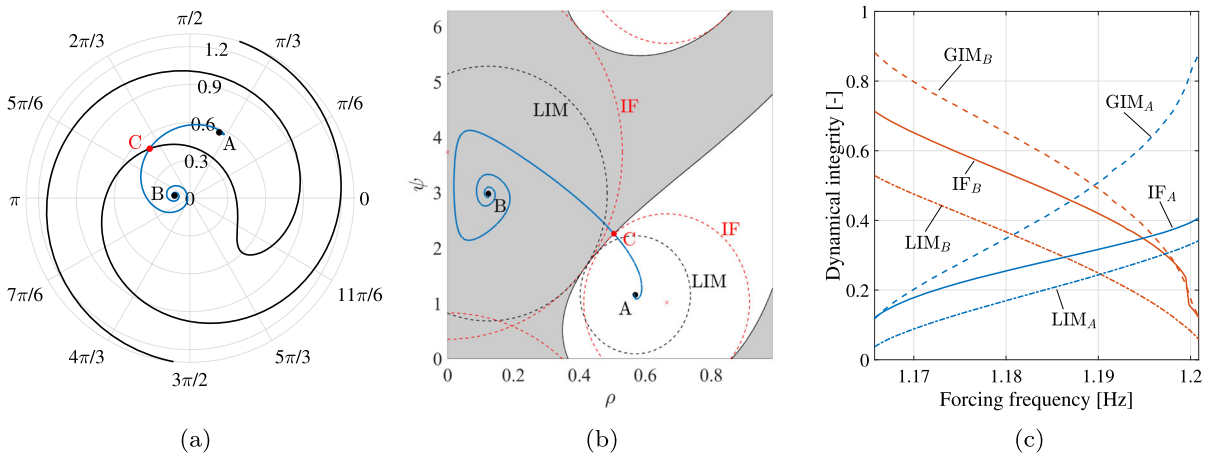

Fig. 5 **a** Phase portrait in the ψ, ρ space in polar coordinates for $\Omega = 1.8 \times 2\pi$ [rad/s] and excitation amplitude 0.32 %; A, B and C mark the two stable and the unstable equilibria, respectively; black lines depict BoA boundaries, while blue lines trajectories from the unstable to the stable equilibria. **b** Phase portrait in the ψ, ρ space in Cartesian coordinates; the red circles indicate the IF and the black ones the LIM. **c** Trends of the IF, LIM, and GIM of the equilibria A and B for varying forcing frequency and excitation amplitude 0.32 %

are represented by solid black lines in the polar phase space in Fig. 5a.

As in the beam example, dynamical integrity measures are computed on a Cartesian representation of the phase space, limiting ψ between 0 and 2π, while ρ between 0 and $\rho_{\max} = 0.9854$, where $\rho_{\max}$ is the largest amplitude for which the ROM is trusted. Figure 5b depicts the considered dynamical integrity measures of the two coexisting steady-state solutions for $\Omega = 1.8 \times 2\pi$ [rad/s] and excitation amplitude 0.32 %. The black circles mark the LIM, the red ones the IF, while the white and gray areas correspond to the GIM of the high amplitude and low amplitude solutions, respectively. The LIM is computed as the minimal distance between each stable equilibrium point and any point of the BoA boundary. The IF is the radius of the largest circle fully included in the basin of attraction of a solution (allowing the circle to be partially outside the considered portion of the phase space but not its center). The GIM is measured as the ratio between the BoA area of each solution and the total considered area of the phase space.

Figure 5c depicts the trend of the dynamical integrity measures over the frequency range having multiple stable steady-state solutions. The higher amplitude solution (A) merges with the unstable one at the lower limit of the considered forcing frequency, while the lower one (B) also merges with the unstable solution but at the higher frequency range limit. The trend of the three dynamical integrity measures is consistent with this observation; they increase with the frequency for the higher amplitude solution (A) and decrease for the lower amplitude solution (B). The LIM and IF curves proceed almost in parallel, while the GIM has larger variations in the considered frequency range. From an engineering perspective, especially the LIM and the IF provide valuable information regarding the robustness of each solution against external perturbations. As regards BoAs competition and the relative position of the integrity profiles obtained with the different measures, similar considerations hold to those made for the von Kármán beam .

3.3 Airfoil undergoing flutter instability subject to harmonic excitation

The third investigated system consists of an airfoil undergoing flutter instability and subject to harmonic excitation. A classical planar pitch-and-plunge model is used to characterize the airfoil motion, as illustrated in Fig. 6 and better described in [76]. Recently, aerodynamic flutter has been analyzed experimentally with SSM identified from processing videos [60].

The geometrical parameters of the airfoil are the semichord b, the chord c, and the lifting surface S.

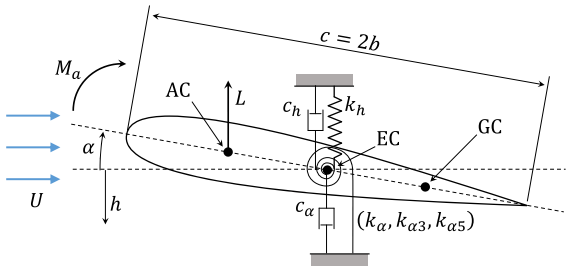

Fig. 6 Mechanical model of the pitch-and-plunge airfoil

GC is the gravity center, EC the elastic center, and AC the aerodynamic center. e marks the distance between AC and EC. The inertial terms of the airfoil include the mass M, the moment of inertia I_α, and the static moment S_a. The static moment S_a is equal to Mx_{CG}, where x_{CG} corresponds to the distance between GC and EC. The plunge motion is characterized by the linear stiffness k_h and damping c_h. The pitch mode is characterized by the stiffness coefficients k_α (linear), $k_{\alpha 3}$ (cubic) and $k_{\alpha 5}$ (fifth order), and the linear damping coefficient c_α. Nonlinear terms take into account structural nonlinearities of geometric or localized nature that can arise in the aeroelastic system, as illustrated also in [3,77–79].

The dynamics of the model is governed by the following non-dimensional equations of motion:

$$\dot{\mathbf{x}} = \mathbf{A}\mathbf{x} + \mathbf{b}(\mathbf{x}) + f_0\mathbf{f}\cos(\omega t), \tag{6}$$

where

$$\begin{aligned}
\mathbf{x} &= \begin{bmatrix} y \\ \alpha \\ \dot{y} \\ \dot{\alpha} \end{bmatrix}, \ \mathbf{b} = -\begin{bmatrix} 0 \\ 0 \\ \mathbf{M}^{-1}\begin{bmatrix} 0 \\ \xi_{\alpha 3}\alpha^3 + \xi_{\alpha 5}\alpha^5 \end{bmatrix} \end{bmatrix}, \\
\mathbf{A} &= \begin{bmatrix} \mathbf{0} & \mathbf{I} \\ -\mathbf{M}^{-1}\mathbf{K} & -\mathbf{M}^{-1}\mathbf{C} \end{bmatrix}, \ \mathbf{M} = \begin{bmatrix} 1 & x_\alpha \\ x_\alpha & r_\alpha^2 \end{bmatrix}, \\
\mathbf{K} &= \begin{bmatrix} \Omega^2 & \beta u^2 \\ 0 & r_\alpha^2 - \nu u^2 \end{bmatrix}, \ \mathbf{C} = \begin{bmatrix} \zeta_h + \beta u & 0 \\ -\nu u & \zeta_\alpha \end{bmatrix},
\end{aligned} \tag{7}$$

α marks the pitch rotation, and y indicates the heave displacement; displacement is non-dimensionalized in relation to the semichord of the airfoil b, while the time to the pitch natural frequency $\omega_\alpha = \sqrt{k_\alpha / I_\alpha}$. Ω is the ratio between the natural frequencies in heave and pitch, r_α and x_α are the non-dimensional inertia coefficients, β and ν are the non-dimensional aerodynamic parameters, ζ_h and ζ_α the pseudo-damping ratio in heave and pitch, respectively, $\xi_{\alpha 3}$ and $\xi_{\alpha 5}$ are the non-dimensional stiffness coefficients. u is the non-dimensional flow velocity, which is utilized as a bifurcation parameter during the analysis. We address the interested reader to [3] for more details on the system parameters and their meaning. The same system was also studied in [79].

Additionally, we include a small harmonic forcing term in the system, assumed acting on the first vibration mode. Here, f_0 is the forcing amplitude, ω is the non-dimensional forcing frequency and $\mathbf{f}$ is the forcing vector which is considered to be aligned to the first mode.

The utilized parameter values are $\beta = 0.2$, $\nu = 0.08$, $x_\alpha = 0.2$, $r_\alpha = 0.5$, $\Omega = 0.5$, $\zeta_\alpha = 0.01$, $\zeta_h = 0.01$, $\xi_{\alpha 3} = -1$ and $\xi_{\alpha 5} = 20$. The forcing frequency was fixed at $\omega = 0.85\sqrt{2}$, a value that avoids resonances for the flow speed u of interest. The forcing was assumed to be perfectly modal, acting on the first vibration mode.

For a critical flow velocity ($u_{\text{AH}} = 0.9331$), the unforced system undergoes a subcritical Andronov-Hopf bifurcation, generating a branch of unstable periodic solution, as illustrated in Fig. 7a . The branch then turns back at a fold bifurcation, after which the periodic solutions become stable. Between the fold and the Andronov-Hopf bifurcations the system is bistable, presenting coexisting equilibrium and periodic stable solutions.

If a harmonic excitation is included in the system, the equilibrium points become periodic solutions, and the periodic solutions become quasiperiodic ones, as shown in Fig. 7b. The Andronov-Hopf bifurcation becomes a Neimark-Sacker one and moves to slightly smaller flow velocity values u. Additionally, the fold bifurcation moves to slightly higher flow velocities u, reducing the range of bistability.

In Figs. 7a and b, stable solutions are obtained through direct numerical simulations and unstable periodic solutions through the shooting method coupled with a pseudo-arclength continuation. Conversely, unstable quasiperiodic solutions of the full system are obtained by identifying a boundary of a BoA through a bisection method. Trajectories initiated on the boundary dwell in close proximity to the unstable quasiperiodic solution before converging to one of the attractors. Analyzing this transient dynamics enables us to

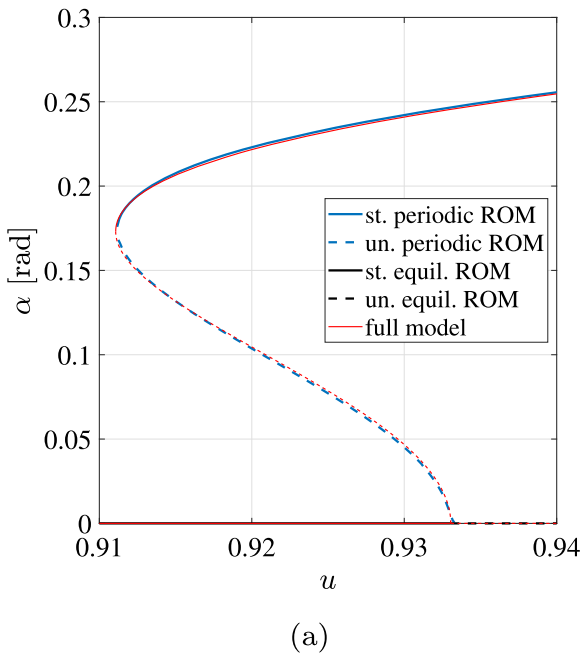

(a)

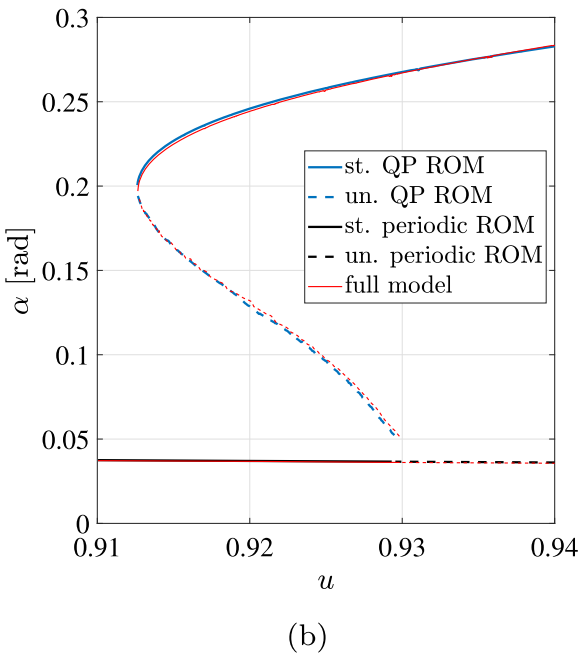

(b)

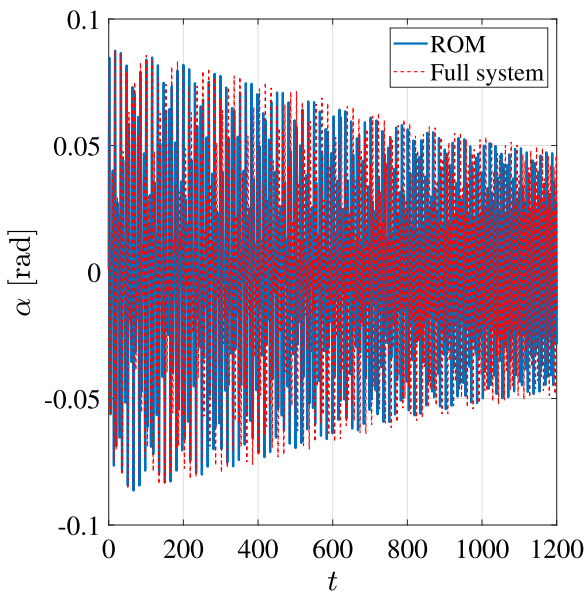

(c)

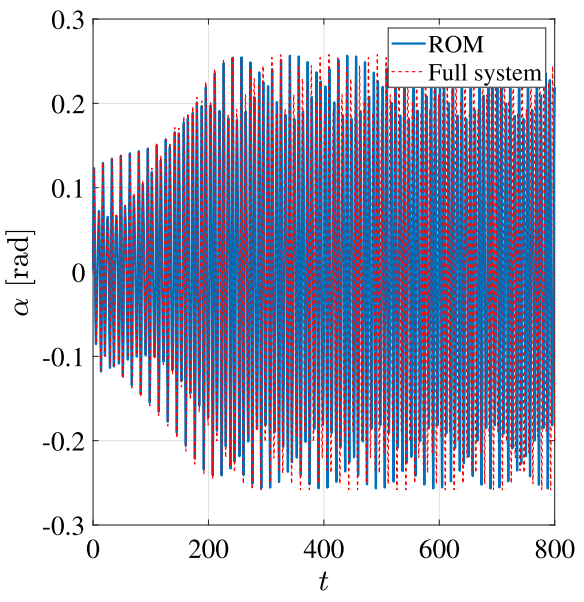

(d)

Fig. 7 **a**, **b** Bifurcation diagram of the unforced **a** and forced **b** system ($f_0 = 0.03$, $\omega = 0.85\sqrt{2}$); blue and black lines: ROM, red lines: full model. **c**, **d** Comparison of time series of the ROM and full model for $u = 0.915$, $f_0 = 0.03$, $\omega = 0.85\sqrt{2}$, $\mathbf{x}(0) = [0, 0.1]^\intercal$ **c** and $\mathbf{x}(0) = [0, 0.15]^\intercal$ **d**

estimate the amplitude of the unstable quasiperiodic solutions with good accuracy.

The considered mathematical model for the system, as in Eq. (6), is already a ROM. Accordingly, a further reduction of the system through `SSMLearn` is clearly less meaningful than in the previously considered examples. However, the fact that the original system already has limited dimension allows us to validate the dynamical integrity analysis and evaluate the accuracy of the `SSMLearn` ROM's global dynamics, an operation unfeasible for the other examples. Besides, the mathematical model is used uniquely to generate trajectories; therefore, its low dimension does not diminish the relevance of the method implemented.

For the system under study, the identification of the `SSMLearn` ROM is different than in the previous examples as the aim is to capture different dynamical regimes. While for the von Kármán beam and the sloshing water system all parameters of the unforced system were constant, in this case we aim to obtain a ROM valid for a given range of the flow velocity u, which makes the reduction parametric. Specifically, the vector field gets parametric dependance on u and the adopted system identification procedure, still performed on the unforced system, is as follows. First, a limit cycle oscillation is obtained through a direct numerical simulation of the full system for a post-critical flow velocity ($u = 0.98$) with initial condition close to the unstable linear subspace of the origin. Then, one point of the limit cycle is used as the initial condition as it should reasonably lay close to the slow stable SSMs of the origin. From here, three simulations are performed for smaller flow velocities belonging to the stable region of the trivial solution, namely $u = 0.85$, 0.875, and 0.9. Then, the trajectory data describing different dynamical regimes are used to fit a two-dimensional fifth-order polynomial differential equation, allowing a second-order variation of each coefficient with respect to the bifurcation parameter u.

The ROM is mathematically expressed as

$$\begin{bmatrix} \dot{x}_1 \\ \dot{x}_2 \end{bmatrix} = \sum_{\substack{j+k+l=1,\\ j+k\neq 0,\, l\leq 2\\ j\geq 0,\, k\geq 0,\, l\geq 0}}^{5} x_1^j x_2^k p^l \begin{bmatrix} \varphi_{1,j,k,l} \\ \varphi_{2,j,k,l} \end{bmatrix} + \tilde{\mathbf{f}}\, f_0 \cos(\omega t)\,, \tag{8}$$

where $\varphi_{1,j,k,l}$ and $\varphi_{2,j,k,l}$ represent the coefficients identified during the ROM construction, p is the bifurcation parameter, defined as $p = u - u_{\mathrm{AH}}$, such that the Andronov-Hopf bifurcation occurs for $p = 0$, f_0 and ω are the forcing amplitude and frequency, respectively, and $\tilde{\mathbf{f}}$ indicates which mode is excited. In this study, $\tilde{\mathbf{f}}$ is always fixed at $[1 \quad 0]^\intercal$; coefficients $\varphi_{1,j,k,l}$ and $\varphi_{2,j,k,l}$ are provided in the codes accompanying this paper.

Figure 7 shows a comparison of the dynamics exhibited by the ROM and full models. Figure 7a depicts the bifurcation diagram of the unforced system, while Fig. 7b refers to the forced system ($f_0 = 0.03$). Both of them show an excellent agreement between the full and ROM. Figures 7c and d compare two trajectories obtained for the same parameter values but different initial conditions ($f_0 = 0.03$, $u = 0.915$, $\mathbf{x}(0) = [0, 0.1]^\intercal$ in Fig. 7c and $\mathbf{x}(0) = [0, 0.15]^\intercal$ in Fig. 7d). Also in this case, the matching between the ROM and the full model is excellent.

We now aim to study the dynamical integrity of the ROM. The attention is focused on the forced system. In the bistable region of the system, the unstable quasiperiodic solution exactly corresponds to the boundary of the BoAs. In fact, it divides the phase space into two parts: an outer region that is the BoA of the stable quasiperiodic solution and an inner region that is the BoA of the periodic solution, as illustrated in Fig. 8a. Additionally, the unstable quasiperiodic solution can be easily found through reverse-time numerical integration. We note that this simple identification of the BoA can be done only because the system is three-dimensional (x_1, x_2, and the phase of the excitation); accordingly, boundaries of the BoA are marked by two-dimensional surfaces. In the full system (five-dimensional), the unstable quasiperiodic solution is only a two-dimensional object that lies on the four-dimensional boundaries of the BoA; therefore, it does not fully identify it.

The analysis of the dynamical integrity is limited to the LIM, which, despite being the most rapid to be computed, provides a significant quantification of a solution's dynamical integrity, especially for simple geometries of the BoA as in the present case. The LIM is measured on a stroboscopic Poincaré section of the phase space, sampled every excitation period. Accordingly, periodic solutions are reduced to points and quasiperiodic ones to closed curves. The LIM of the periodic solution is measured as the minimal distance between the periodic solution and the unstable

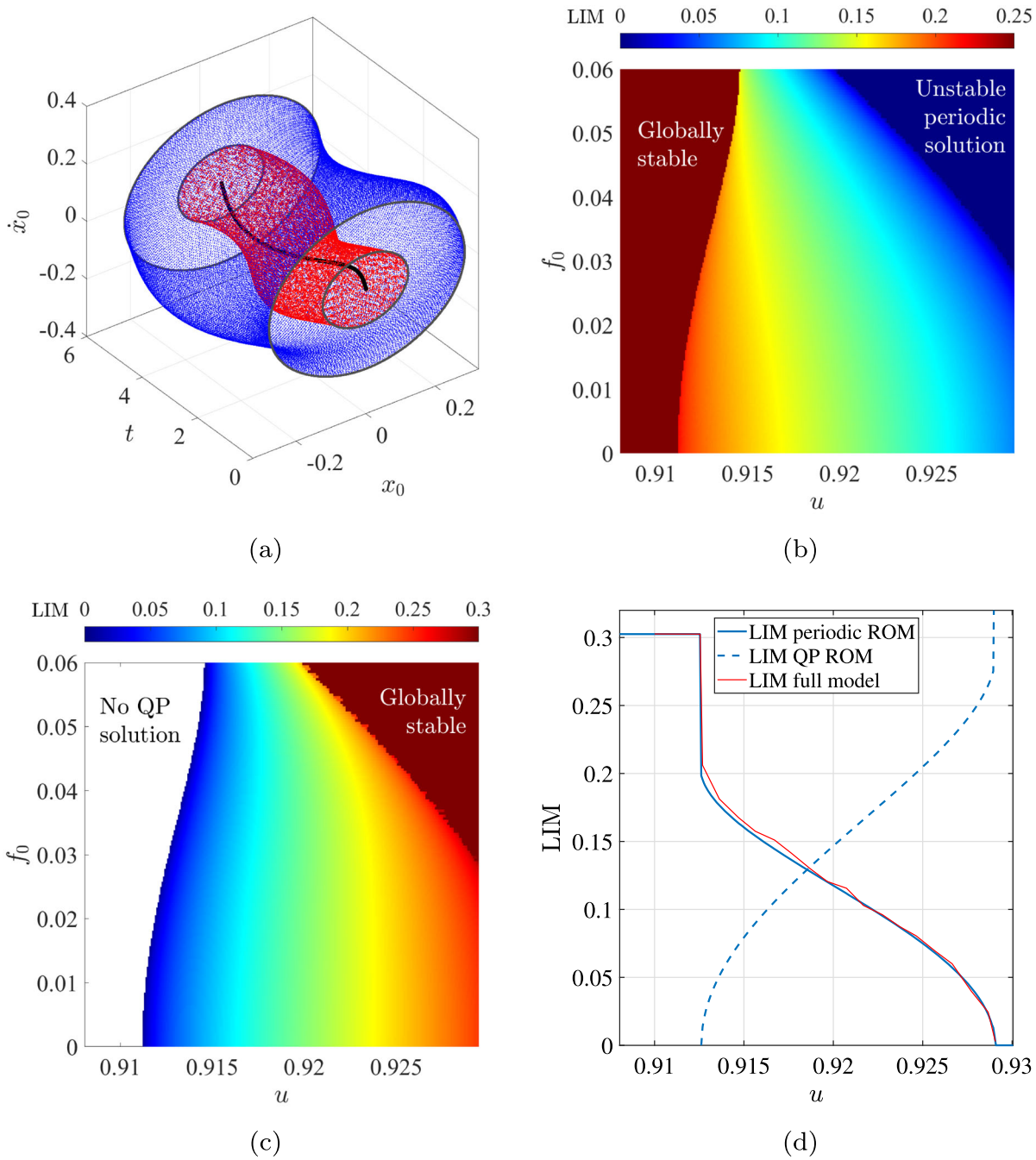

Fig. 8 **a** Solutions of the ROM in Eq. (8) for $f_0 = 0.03$ and $\omega = 0.85\sqrt{2}$; blue: stable quasiperiodic solution, red: unstable quasiperiodic solution, black: stable periodic solution. **b** LIM of the periodic solution of the forced system ($\omega = 0.85\sqrt{2}$). **c** LIM of the quasiperiodic solution of the forced system ($\omega = 0.85\sqrt{2}$). **d** comparison between the LIM of the forced system's periodic solutions for the full and ROM; solid blue line: ROM, red line: full model, dashed blue line: quasiperiodic solution for the ROM ($f_0 = 0.03$, $\omega = 0.85\sqrt{2}$)

quasiperiodic one. Regarding the stable quasiperiodic solution, the LIM is defined as the radius of the largest hypersphere centered on any point of the solution and entirely included in its BoA. In this case, limiting the analysis to a Poincaré section, the hypersphere is reduced to a circle, and the LIM can be measured as the minimal distance between any couple of points of the two quasiperiodic solutions, the stable and the unstable one.

Results of the computation are depicted in Figs. 8b and c for variations of the flow velocity u and forcing amplitude f_0. The two figures show how the range of bistability shrinks when the forcing amplitude is increased. Besides, the LIM overall scenarios of the stable periodic and quasiperiodic solutions are somehow exchanged with each other. Namely, the LIM of the periodic solution decreases while approaching the Neimark-Sacker bifurcations; conversely, the LIM of the quasiperiodic solution is zero at the fold bifurcation and increases for higher flow velocity values. On the left of the fold bifurcation, the periodic solution is globally stable, while on the right of the Neimark-Sacker bifurcation, the quasiperiodic solution is globally stable.

The LIM of the periodic solutions computed for the ROM is compared to the one obtained for the full model, as illustrated in Fig. 8d. For the full model, the LIM was estimated through the `DynIn` toolbox [35,36], which enables to rapidly compute the LIM of steady-state solutions without requiring to compute the full BoA. The `DynIn` toolbox iteratively estimates the LIM by measuring the minimal distance between the target steady-state solution and non-converging trajectories. The analysis was performed in a four-dimensional stroboscopic Poincaré section of the phase space. The full and the SSM-based ROM produced two LIMs not directly comparable because the full model requires scaling of the different dimensions to define a hypersphere (see [35] for more details). Accordingly, a constant scaling factor of 2.18, determined euristically, was applied on the LIM computed for the full model as depicted in Fig. 8d. After this scaling, the matching between the full and the ROM is excellent. Irregularities of the curve relative to the LIM for the full model are due to the `DynIn` toolbox, which does not provide an exact value but only an approximation. From the phenomenological viewpoint, the sharp fall down of the LIM profile of the periodic solution, occurring at the flow velocity value where the quasiperiodic solution is established via fold bifurcation (see Fig. 7b), corresponds to an abrupt decrease of robustness of the former with respect to finite, though small, variations of initial conditions or, in more general terms, of safety of its BoA with respect to an extremely small variation of the considered control parameter. The dashed blue line in Fig. 8d represents the LIM of the quasiperiodic solution for the ROM. Similar to the behavior observed for the previous systems, we note mirrored trends in the LIMs of the two coexisting solutions—in this case, the periodic and quasiperiodic solutions. The flow velocity at which the two blue lines intersect in Fig. 8d indicates the condition where the unstable quasiperiodic solution is equidistant from the two stable solutions.

A further validation of the accuracy of the global dynamics exhibited by the ROM with respect to the full model is proven by the comparison of the BoAs of the two systems. These are illustrated in Fig. 9 for various values of the flow speed u and $f_0 = 0.03$. In this case, the BoAs are obtained through direct numerical simulations on a grid of initial conditions. The gray (white) regions mark the BoA of the reduced model's periodic (quasiperiodic) solution, while the red lines indicate the BoA boundaries for the full model. The matching between the two models is excellent for lower flow speed (Fig. 9a), while it slightly worsens for higher flow speed (Fig. 9d). The worsening is due to the flow velocities used for the model identification, all chosen below the fold bifurcation. Accordingly, for higher flow velocities, the system is farther from the flow velocity range used for the identification, unsurprisingly reducing accuracy.

3.4 Von Kármán beam undergoing dynamic buckling

The fourth analyzed system is a pinned-pinned von Kármán beam subject to a constant compressive axial load, as illustrated in Fig. 10a. The beam, assumed to be made of steel, has a density $\rho = 7850\,[\mathrm{kg/m^3}]$, a Young's modulus $E = 1.9 \times 10^{11}\,[\mathrm{Pa}]$, viscous damping rate $\nu = 7 \times 10^6\,[\mathrm{kg\,m/s}]$, length $L = 2\,[\mathrm{m}]$, and a squared cross section of width $w = 0.05\,[\mathrm{m}]$ and height $h = 0.01\,[\mathrm{m}]$. The final element model of the structure consists of 13 nodes, each with axial, transversal, and rotational DoF. Considering the boundary condition constraints, the model has a total of 72 DoFs. This system was previously investigated in [61,80], where

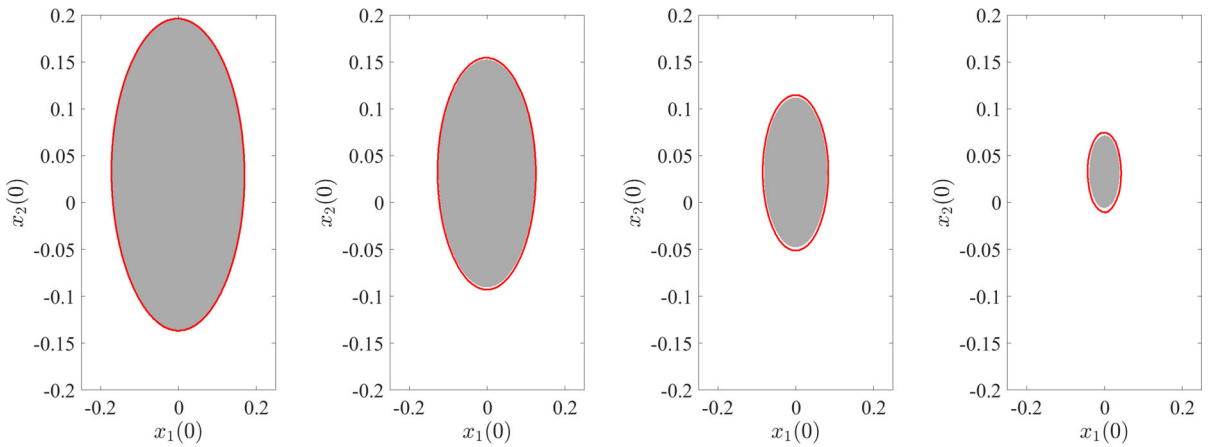

Fig. 9 Basin of attraction of the full model (red line) and of the ROM (black surface), for $f_0 = 0.03$ and $\omega = 0.85\sqrt{2}$. Initial conditions refer to the reduced system

further details regarding the model and the SSM identification procedure can be found.

The system is subject to a static axial load F, 10 % larger than its first critical axial load, i.e.,

$$F = 1.1\pi^2 E\frac{I}{L^2} = 1.1\frac{\pi^2 E}{12}\frac{bh^3}{L^2}, \tag{9}$$

resulting in three equilibrium configurations: two stable symmetric buckled states and one unstable, axially compressed state.

Differently from the previous examples, the SSM in this case is a 2-dimensional mixed-mode one emanating from the unstable solution, which is a saddle point whose first eigenvalues are $\lambda_1 = 11.06$ and $\lambda_2 = -11.10$. Four truncated trajectories are employed for the SSM identification, with initial conditions obtained by applying a transverse force at the midpoint of the beam x_M and subsequently releasing the system. The applied forces for these four trajectories are 10×10^{-4}, -10×10^{-4}, 10×10^{4}, and -10×10^{4} [N], respectively. The first two excitations generate in-well trajectories around one of the stable buckled configurations, while the third and fourth induce large-amplitude oscillations surrounding all three equilibria before settling into one of the stable states. Three observables of the system are considered: the transverse displacement and velocity of the midpoint, and the axial displacement of the right endpoint.

A seventh order polynomial is fitted to the data points from these trajectories, parametrized using the eigenspace coordinates of the unstable equilibrium, yielding estimates of the SSMs. The resulting ROM is then constructed by projecting the training data onto the identified manifold. Subsequently, a harmonic transverse force is applied at the beam's midpoint, leading to the following reduced-order system of differential equations:

$$\begin{bmatrix}\dot{\eta}_1\\ \dot{\eta}_2\end{bmatrix} = \begin{bmatrix}\lambda_1\eta_1\\ \lambda_2\eta_2\end{bmatrix} + \sum_{j+k=2}^{7}\eta_1^j\eta_2^k\begin{bmatrix}\varphi_{1,j,k}\\ \varphi_{2,j,k}\end{bmatrix} + \\ +\tilde{\mathbf{f}}\,f_0\cos(\omega t)\,, \qquad \tilde{\mathbf{f}} = \begin{bmatrix}-0.616\\ -0.618\end{bmatrix}, \tag{10}$$

where $\varphi_{1,j,k}$ and $\varphi_{2,j,k}$ represent the 2×33 nonlinear coefficients identified during the ROM construction, while f_0 and ω represent the forcing amplitude and frequency, respectively. The vector $\tilde{\mathbf{f}}$ denotes the projection of the external force onto the modal coordinates.

The ROM dynamics is qualitatively similar to that of a harmonically excited Duffing oscillator with negative linear and positive cubic stiffness [81,82]. For relatively small forcing amplitude, the system behaves as two symmetric softening resonators, each operating independently around one of the two stable equilibria. This behavior is captured in the FRC in Fig. 10b,

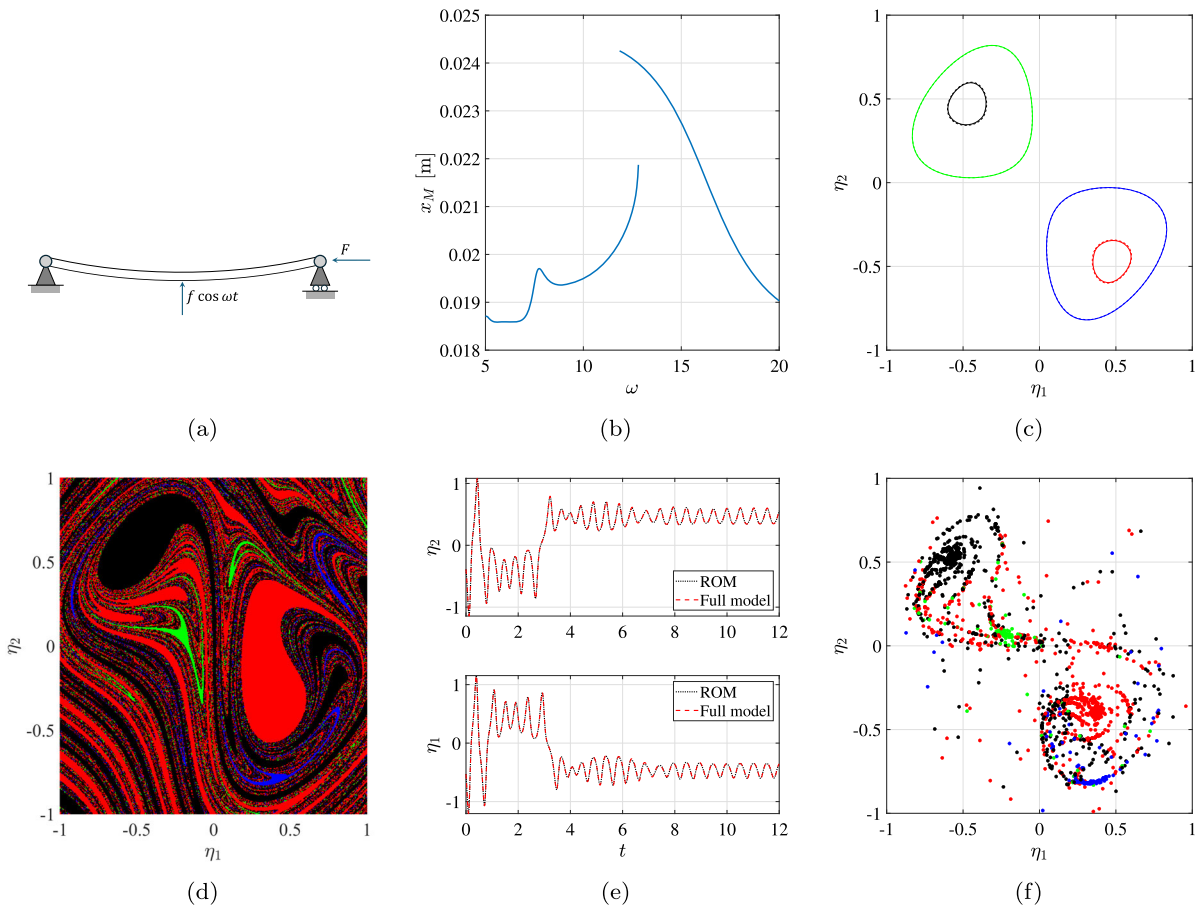

Fig. 10 **a** Mechanical model of the beam undergoing buckling. **b** Frequency response of the ROM projected on real coordinates for $f_0 = 1$ (unstable solutions are omitted); vertical axis marks the maximal transeversal displacement of the beam central point (x_M). **c** Attractors of the system for $f_0 = 1$ and $\omega = 12.2$; solid line: SSM-ROM, dashed lines: full model. **d** BoA of the SSM-ROM for the same excitation forcing and frequency; colors correspond to the attractors in panel **c**. **e** Comparative time series of the full (dashed lines) and SSM-ROM (dotted lines). **f** Stroboscopic phase portrait of the full system obtained from 85 trajectories with random initial conditions; colors correspond to the attractors in panel **c**

obtained from the ROM. For excitation frequencies slightly below the in-well natural frequency, two periodic solutions coexist in each potential well, yielding four periodic solutions in total. These are depicted in Fig. 10c for a forcing amplitude of $f_0 = 1$ and excitation frequency $\omega = 12.2$.

Figure 10c also illustrates the excellent agreement between the ROM and the full-order model in predicting the system's attractors. The ROM solutions (solid lines) are virtually indistinguishable from those of the full model (dashed lines), when projected onto the SSM.

Although only regular attractors are observed for the considered parameter values, the transient dynamics remain complex. When the system's energy exceeds the potential barrier between wells, transient chaotic motions emerge, generating a fractal BoA, as shown in Fig. 10d for the ROM. The colors in Fig. 10d indicate the BoAs corresponding to the steady-state solutions in Fig. 10c. This chaotic transient behavior and the associated fractality of the BoAs further underscore the effectiveness of SSM-based model reduction, as previously discussed in [61,80].

Figure 10e displays time series for two trajectories converging to the black and red periodic solutions in

Table 1 GIM obtained for the full and ROM of the buckled beam

	GIM full	GIM ROM
red	0.42	0.49
blue	0.07	0.03
black	0.45	0.44
green	0.06	0.04

Fig. 10c, respectively, for $f_0 = 1$ and $\omega = 12.2$. Once again, the excellent agreement between the ROM and full model validates the ROM's accuracy, not only for steady states but also for transient dynamics, which is essential for reliably estimating the system's dynamical integrity.

Although generating a high-resolution BoA for the full model is computationally prohibitive, a draft estimate can be obtained by simulating a limited number of trajectories with random initial conditions and recording their intersections with a stroboscopic Poincaré section, as illustrated in Fig. 10f. The color coding in this figure matches that of Fig. 10d to facilitate direct comparison. A quantitative comparison of the BoAs of the two models can be performed using the GIM, computed as the fraction of trajectories converging to each attractor, relative to the total number of computed trajectories. The results are summarized in Table 1.

Both the GIM estimates and the visual inspection of the BoAs indicate that, for the selected parameter values, the low-amplitude periodic solutions (red and black) dominate the dynamical scenario, while the probabilities of reaching the large-amplitude solutions (blue and green) are significantly lower. A good agreement between the full model and ROM is observed for the GIM values of the low-amplitude attractors. The larger discrepancies for the rare, high-amplitude solutions may not necessarily indicate inaccuracies in the ROM but could instead result from the limited number of simulated trajectories in the full model, leading to a poor statistical representation of these infrequent outcomes.

The low dimensionality of the ROM permits the computation of additional DI measures at reasonable computational cost. This process can be further accelerated using the `DynIn` toolbox [35,36,63], which efficiently computes the LIM, as discussed in Sect. 3.3. The LIM is first evaluated for a fixed forcing amplitude $f_0 = 1$ while varying the excitation frequency ω (Fig. 11a), and then for a fixed excitation frequency $\omega = 12.2$ while increasing the forcing amplitude f_0 (Fig. 11b). It is worth noting that the LIM computations were performed using the algorithm proposed in [35], which analyzes periodic solutions by reducing them to fixed points through their stroboscopic maps, in contrast to the approach in [63], which considers the full periodic trajectories directly.

Figure 11a depicts the LIM calculated for the green and black periodic orbits in Fig. 10c. For $\omega < 11.9$, only the low-amplitude solutions exist (one in each potential well), while for $\omega > 12.8$ only the large-amplitude ones persist. Between these values, two periodic solutions coexist in each potential well, for a total of four steady-state solutions.

For $\omega < 11.9$, basin escape occurs only if the potential well barrier is overcome, making the in-well solutions relatively robust. However, as the excitation frequency increases, the oscillation amplitude also grows (see Fig. 10b), progressively eroding the LIM as the distance between the periodic solutions under study and the potential well barrier decreases. For $\omega > 11.9$, as the larger-amplitude periodic solution emerges, the LIM of the small-amplitude one is further reduced, ultimately reaching zero when the low-amplitude solution ceases to exist. We also note a sudden decrease in the LIM around $\omega \approx 7.6$, in correspondence of the superharmonic resonance visible in Fig. 10b.

The right LIM branch in Fig. 11a refers to the large-amplitude periodic solution (right branch in Fig. 10b, green line in Fig. 10c). For large excitation frequency ω, this solution is robust because of its small amplitude; however, as the excitation frequency decreases, its LIM also diminishes as the solution becomes larger and moves closer to the potential well barrier. For $\omega < 12.8$, as the small-amplitude periodic solution appears, the LIM of the larger-amplitude solution further decreases, until it reaches zero as the corresponding periodic solution disappears. The reason for the peak observed in the LIM curve around $\omega \approx 18$ is not immediately obvious and may be related to the phase selected for the stroboscopic mapping. A detailed analysis of this phenomenon lies beyond the scope of this study. We note that the LIM curves appear particularly noisy around the resonance peak; this is likely due to the increased relevance of transient chaotic trajectories in that region.

Figure 11b shows the trend of the LIM for the periodic solution in one of the potential wells as the forcing amplitude f_0 is increased, for a fixed excitation

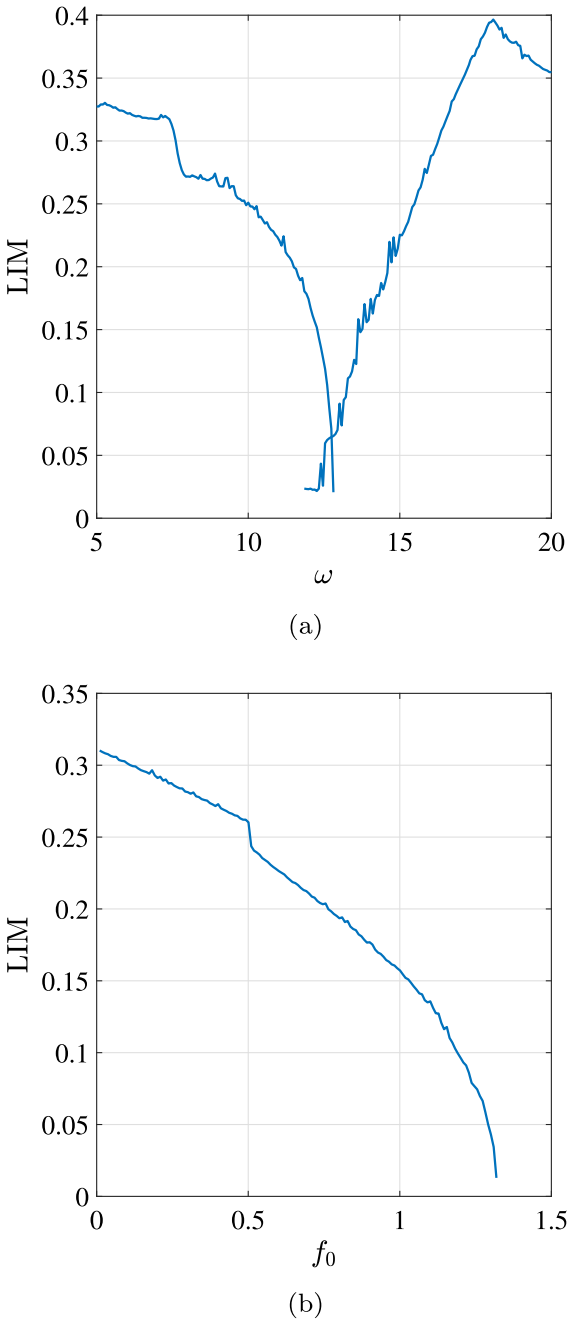

Fig. 11 The figure refers to the LIM calculated for the buckled beam. **a** LIM computed through the `DynIn` toolbox for $f_0 = 1$ and varying excitation frequency ω. **b** LIM for $\omega = 12.2$ and varying excitation amplitude f_0, computed for the low amplitude solution. The LIM is computed for the periodic solutions in the left potential well

frequency $\omega = 12.2$. For small f_0 values, the solution is robust thanks to its low amplitude and relatively large distance from the potential well barrier. As f_0 increases, the LIM decreases while the amplitude of the periodic solution grows. A sudden jump is observed for $f_0 = 0.5$, corresponding to the appearance of the large-amplitude periodic solution coexisting within the same potential well. Further increasing f_0, the LIM continues to decrease, eventually reaching zero when the algorithm is no longer able to identify a stable periodic solution, most likely due to its loss of stability, and the emergence of stable chaotic attractors.

Overall, the analysis of this system illustrates the potential of the SSM reduction technique for dynamical integrity estimation, with further computational advantages when coupled with dedicated DI estimation tools such as the `DynIn` toolbox.

4 Conclusions

This study illustrated how the SSM theory can be exploited to analyze the global dynamics of a system and assess the dynamical integrity of its attractors. Four different systems were investigated: a finite element model of a clamped-clamped von Kármán beam, an experimental setup of sloshing water in a tank, a reduced model of a forced pitch-and-plunge airfoil undergoing flutter, and an axially compressed von Kármán beam undergoing dynamic buckling. Each of them presented specific challenges. The clamped-clamped von Kármán beam has many DoF, making it extremely challenging to study its dynamical integrity directly. Regarding the sloshing water example, its experimental nature makes it inherently challenging to study its dynamical integrity. In contrast, the dynamical integrity of the airfoil can be studied numerically (although at a relatively high computational cost). A major challenge for this system was obtaining a parametric SSM-based ROM. Finally, the von Kármán beam undergoing dynamic buckling exhibits transient chaotic motion, leading to fractal BoAs, which makes the DI analysis particularly demanding, especially considering the large dimensionality of the model.

For the first two cases, the SSM-based ROMs were two-dimensional, and the existing periodic steady-state solutions were reduced to fixed points, making the dynamical integrity analysis trivial. Regarding the pitch-and-plunge system, the ROM was three-dimen-

sional; nevertheless, since the unstable steady-state solution completely divided the phase space in two regions, the dynamical integrity of the stable solutions did not require extensive numerical simulations in this case either. The computational advantage obtained with respect to classical approaches, such as the cell-mapping method, is significant and made possible only because of model reduction. Conversely, the ROM of the axially compressed beam, although also three-dimensional, did not allow for direct DI calculation, as the steady-state solutions did not completely separate the BoAs. In this case, the `DynIn` toolbox was employed to accelerate the LIM estimation process, bypassing the BoA identification.

Overall, this study illustrated how the computational cost of dynamical integrity analysis can be almost completely eliminated—compared to traditional methods—if a proper model reduction is implemented, making it feasible for systems that are difficult to treat with conventional techniques. In particular, the DI estimation of the full clamped-clamped beam model would likely require several days of computation, while the proposed method completed both the model reduction and DI calculation in a matter of seconds. For the pitch-and-plunge airfoil model, although a DI analysis of the full system would be feasible, accounting for variations in two parameters would probably take several hours, if not days, while the proposed method completed this task in under a few minutes. Similarly, for the axially compressed von Kármán beam, the computation time for the DI calculation, including the ROM identification, was in the order of a few minutes on a standard laptop, whereas the same analysis on the full system would likely take weeks with equivalent hardware. Regarding the sloshing water model, traditional methods are incapable of thoroughly computing its DI. In general, the improvement in computational time achieved by the proposed approach amounts to several orders of magnitude. Additionally, the accuracy of the approach was demonstrated for the pitch-and-plunge airfoil and the buckling beam examples. These results suggest that the adopted technique can potentially be a valuable tool for engineering design and testing.

Limitations of the study and opportunities for future developments are primarily related to the systems selected to demonstrate the potential of SSM-based ROMs for the global analysis of high-dimensional systems. For example, non-smooth systems or systems with multiple interacting modes pose challenges to the SSM model reduction; however, recent developments suggest that the method can be extended also to those challenging cases [83,84].

Another aspect not discussed in this study is the required order of the SSM reduction to obtain accurate results. In this respect, general considerations are valid also for this specific application, i.e., increasing the order tends to improve accuracy, but an excessively high order might generate overfitting.

Additionally, it should be noted that the provided values for the dynamical integrity measures are not particularly meaningful in absolute terms, as it is not straightforward to relate them quantitatively to the actual perturbations a system can withstand [85]. Nevertheless, their trends observed for variations in parameter values clearly identify which parameter regions can be considered safe and which cannot, providing valuable information for engineering design.

In future studies, we plan to apply the same technique to an experimental setup of a buckling system subject to harmonic excitation, similarly to the fourth case study. This test will enable us to fully evaluate the potentiality of the adopted technique for global stability assessment.

Our long-term objective is to develop tools that enable the rapid investigation of the dynamical integrity of large dimensional and experimental systems, untreatable with conventional methods. These tools aim to make dynamical integrity analysis an accessible component of engineering practice, empowering engineers and practitioners to enhance safety in design.

Author contributions G.H. and M.C. conceived the research, wrote the main manuscript text and prepared the figures. M.C. prepared the code for SSM reduction. G.H. prepared the code for dynamical integrity calculation. G.R. reviewed the manuscript.

Funding Open access funding provided by Budapest University of Technology and Economics. The research reported in this paper has been supported by Project no. TKP-6-6/PALY-2021 provided by the Ministry of Culture and Innovation of Hungary from the National Research, Development and Innovation Fund, financed under the TKP2021-NVA funding scheme and by the National Research, Development and Innovation Office (Grant no. NKFI-134496).

Data Availability Statement This study exploits codes available at the GitHub repositories https://github.com/haller-group/SSMLearn https://github.com/haller-group/SSMLearn and https://github.com/GlobalDynamicsRG/DynIn. Data related to the research is available from the authors upon reasonable request.

Code availability This study exploits codes available at the GitHub repositories https://github.com/haller-group/SSMLearn and https://github.com/GlobalDynamicsRG/DynIn.

Declarations

Conflict of interests The authors declare that they have no Conflict of interests.

References

1. Dombovari, Z., Iglesias, A., Molnar, T.G., Habib, G., Munoa, J., Kuske, R., Stepan, G.: Experimental observations on unsafe zones in milling processes. Phil. Trans. R. Soc. A **377**(2153), 20180125 (2019). https://doi.org/10.1098/rsta.2018.0125
2. Dombovari, Z., Stepan, G.: On the Bistable zone of milling processes. Philos. Trans. Royal Soc. A: Math. Phys. Eng. Sci. **373**(2051), 20140409 (2015). https://doi.org/10.1098/rsta.2014.0409
3. Malher, A., Touzé, C., Doaré, O., Habib, G., Kerschen, G.: Flutter control of a two-degrees-of-freedom airfoil using a nonlinear tuned vibration absorber. J. Comput. Nonlinear Dyn. **12**(5), 051016 (2017). https://doi.org/10.1115/1.4036420
4. Li, P., Yang, Y., Lu, L.: Nonlinear flutter behavior of a plate with motion constraints in subsonic flow. Meccanica **49**, 2797–2815 (2014). https://doi.org/10.1007/s11012-014-0041-8
5. Nagy, P.T., Kulcsár, M.: Predicting the energy stability limit of shear flows using weighted velocity components. Phys. Fluids (2023). https://doi.org/10.1063/5.0169594
6. Genda, A., Fidlin, A., Gendelman, O.: On the escape of a resonantly excited couple of particles from a potential well. Nonlinear Dyn. **104**, 91–102 (2021). https://doi.org/10.1007/s11071-021-06312-7
7. Lenci, S., Benedetti, K.C., Rega, G., Gonçalves, P.B.: Stochastic basins of attraction for uncertain initial conditions. J. Sound Vib. **587**, 118488 (2024). https://doi.org/10.1016/j.jsv.2024.118488
8. Arnold, L., Chueshov, I., Ochs, G.: Stability and capsizing of ships in random sea-a survey. Nonlinear Dyn. **36**(2), 135–179 (2004). https://doi.org/10.1023/B:NODY.0000045506.30721.f2
9. Horvath, H.Z., Takacs, D.: Stability and local bifurcation analyses of two-wheeled trailers considering the nonlinear coupling between lateral and vertical motions. Nonlinear Dyn. **107**(3), 2115–2132 (2021). https://doi.org/10.1007/s11071-021-07120-9
10. Habib, G., Epasto, A.: Towed wheel shimmy suppression through a nonlinear tuned vibration absorber. Nonlinear Dyn. **111**(10), 8973–8986 (2023). https://doi.org/10.1007/s11071-023-08314-z
11. Dekemele, K.: Tailored nonlinear stiffness and geometric damping: Applied to a bistable vibration absorber. Int. J. Non-Linear Mech. **157**, 104548 (2023). https://doi.org/10.1016/j.ijnonlinmec.2023.104548
12. Starosvetsky, Y., Gendelman, O.: Vibration absorption in systems with a nonlinear energy sink: nonlinear damping. J. Sound Vib. **324**(3–5), 916–939 (2009). https://doi.org/10.1016/j.jsv.2009.02.052
13. Bureau, E., Schilder, F., Elmegård, M., Santos, I.F., Thomsen, J.J., Starke, J.: Experimental bifurcation analysis of an impact oscillator—determining stability. J. Sound Vib. **333**(21), 5464–5474 (2014). https://doi.org/10.1016/j.jsv.2014.05.032
14. Zhang, L., Stepan, G., Insperger, T.: Saturation limits the contribution of acceleration feedback to balancing against reaction delay. J. R. Soc. Interface **15**(138), 20170771 (2018). https://doi.org/10.1098/rsif.2017.0771
15. Kadar, F., Stepan, G.: Nonlinear dynamics and safety aspects of pressure relief valves. Nonlinear Dyn. **111**(13), 12017–12032 (2023). https://doi.org/10.1007/s11071-023-08484-w
16. Habib, G., Bártfai, A., Barrios, A., Dombovari, Z.: Bistability and delayed acceleration feedback control analytical study of collocated and non-collocated cases. Nonlinear Dyn. **108**(3), 2075–2096 (2022). https://doi.org/10.1007/s11071-022-07308-7
17. Du, Y., Li, Q., Fan, H., Zhan, M., Xiao, J., Wang, X.: Inferring attracting basins of power system with machine learning. Phys. Rev. Res. (2024). https://doi.org/10.1103/PhysRevResearch.6.013181
18. Thompson, J.M.T.: Chaotic phenomena triggering the escape from a potential well. In: Proceedings of the Royal Society of London. A. Mathematical and Physical Sciences **421**(1861), 195–225. (1989) https://doi.org/10.1098/rspa.1989.0009
19. Soliman, M., Thompson, J.: Integrity measures quantifying the erosion of smooth and fractal basins of attraction. J. Sound Vib. **135**(3), 453–475 (1989). https://doi.org/10.1016/0022-460X(89)90699-8
20. Lenci, S., Rega, G.: Optimal control of homoclinic bifurcation: theoretical treatment and practical reduction of safe basin erosion in the helmholtz oscillator. J. Vib. Control **9**(3–4), 281–315 (2003). https://doi.org/10.1177/107754603030753
21. Rega, G., Lenci, S.: Identifying, evaluating, and controlling dynamical integrity measures in non-linear mechanical oscillators. Nonlinear Anal. Theory Methods Appl. **63**(5–7), 902–914 (2005). https://doi.org/10.1016/j.na.2005.01.084
22. Hsu, C.S.: A theory of cell-to-cell mapping dynamical systems. J. Appl. Mech. **47**(4), 931–939 (1980). https://doi.org/10.1115/1.3153816

23. Hsu, C.S.: Cell-to-Cell Mapping: A Method of Global Analysis for Nonlinear Systems, vol. 64. Springer Science & Business Media, NY (2013)
24. Sun, J.Q., Xiong, F.R., Schütze, O., Hernández, C.: Cell Mapping Methods. Springer, Singapore (2018)
25. Markov, A.A.: Extension of the limit theorems of probability theory to a sum of variables connected in a chain. Bulletin of the Imperial Academy of Sciences of St. Petersburg **15**, 135–156 (1906)
26. Kemeny, J.G., Snell, J.L., Knapp, A.W.: Denumerable Markov Chains, 2nd edn. Springer-Verlag, New York (1976)
27. Xiong, F.R., Qin, Z.C., Ding, Q., Hernández, C., Fernandez, J., Schütze, O., Sun, J.Q.: Parallel cell mapping method for global analysis of high-dimensional nonlinear dynamical systems. J. Appl. Mech. **82**(11), 111010 (2015). https://doi.org/10.1115/1.4031149
28. Stender, M., Hoffmann, N.: bSTAB: an open-source software for computing the basin stability of multi-stable dynamical systems. Nonlinear Dyn. **107**(2), 1451–1468 (2022). https://doi.org/10.1007/s11071-021-06786-5
29. Delabays, R., Tyloo, M., Jacquod, P.: The size of the sync basin revisited. Chaos: An Interdiscip. J. Nonlinear Sci. (2017). https://doi.org/10.1063/1.4986156
30. Levin, A.: An analytical method of estimating the domain of attraction for polynomial differential equations. IEEE Trans. Autom. Control **39**(12), 2471–2475 (1994). https://doi.org/10.1109/9.362845
31. Grinberg, I., Gendelman, O.V.: Boundary for complete set of attractors for forced-damped essentially nonlinear systems. J. Appl. Mech. **82**(5), 051004 (2015). https://doi.org/10.1115/1.4030045
32. Virgin, L.N.: Introduction to experimental nonlinear dynamics: a case study in mechanical vibration. Cambridge University Press, Cambridge (2000)
33. Virgin, L.N., George, C., Kini, A.: Experiments on a non-smoothly-forced oscillator. Physica D **313**, 1–10 (2015). https://doi.org/10.1016/j.physd.2015.09.002
34. Zakynthinaki, M.S., Stirling, J.R., Cordente Martínez, C.A., Díaz de Durana, A.L., Quintana, M.S., Romo, G.R., Molinuevo, J.S.: Modeling the basin of attraction as a two-dimensional manifold from experimental data: Applications to balance in humans. Chaos: An Interdiscip. J. Nonlinear Sci. (2010). https://doi.org/10.1063/1.3337690
35. Habib, G.: Dynamical integrity assessment of stable equilibria: a new rapid iterative procedure. Nonlinear Dyn. **106**(3), 2073–2096 (2021). https://doi.org/10.1007/s11071-021-06936-9
36. Szaksz, B., Stepan, G., Habib, G.: Dynamical integrity estimation in time delayed systems: a rapid iterative algorithm. J. Sound Vib. **571**, 118045 (2024). https://doi.org/10.1016/j.jsv.2023.118045
37. Bellman, R.E.: Adaptive Control Processes: A Guided Tour. Princeton University Press, Princeton, NJ (1961)
38. Lenci, S., Rega, G.: Global Nonlinear Dynamics for Engineering Design and System Safety, vol. 588. Springer, Cham (2019)
39. Rega, G.: Nonlinear dynamics in mechanics: State of the art and expected future developments. J. Comput. Nonlinear Dyn. (2022). https://doi.org/10.1115/1.4054112
40. Carr, J.: Applications of Centre Manifold Theory. Springer-Verlag, New York (1981)
41. Guckenheimer, J., Holmes, P.: Nonlinear Oscillations, Dynamical Systems, and Bifurcations of Vector Fields. Springer-Verlag, New York (1983)
42. Shaw, S.W., Pierre, C.: Non-linear normal modes and invariant manifolds. J. Sound Vib. **150**(1), 170–173 (1991). https://doi.org/10.1016/0022-460X(91)90412-D
43. Vakakis, A.F., Manevitch, L.I., Mikhlin, Y.V., Pilipchuk, V.N., Zevin, A.A.: Normal Modes and Localization in Nonlinear Systems. Wiley-Interscience, New York (1996)
44. Haller, G., Ponsioen, S.: Nonlinear normal modes and spectral submanifolds: Existence, uniqueness and use in model reduction. Nonlinear Dyn. **86**, 1493–1534 (2016). https://doi.org/10.1007/s11071-016-2974-z
45. Nayfeh, A.H.: The method of normal forms. John Wiley & Sons (2011)
46. Vizzaccaro, A., Shen, Y., Salles, L., Blahoš, J., Touzé, C.: Direct computation of nonlinear mapping via normal form for reduced-order models of finite element nonlinear structures. Comput. Methods Appl. Mech. Eng. **384**, 113957 (2021). https://doi.org/10.1016/j.cma.2021.113957
47. Nayfeh, A.H.: Perturbation Methods. Wiley-VCH, Weinheim (2008)
48. Nayfeh, A.H.: Reduced-order models of weakly nonlinear spatially continuous systems. Nonlinear Dyn. **16**(2), 105–125 (1998). https://doi.org/10.1023/A:1008281121523
49. Guo, T., Rega, G.: Reduced-order modeling of geometrically nonlinear structures part I: a low-order elimination technique. Nonlinear Dyn. **111**(21), 19629–19654 (2023). https://doi.org/10.1007/s11071-023-08822-y
50. Guo, T., Rega, G.: Reduced-order modeling of geometrically nonlinear structures part II: correspondence and unified perspectives on different reduction techniques. Nonlinear Dyn. **111**(21), 19655–19684 (2023). https://doi.org/10.1007/s11071-023-08745-8
51. Jain, S., Haller, G.: How to compute invariant manifolds and their reduced dynamics in high-dimensional finite element models. Nonlinear Dyn. **107**(2), 1417–1450 (2021). https://doi.org/10.1007/s11071-021-06957-4
52. Cenedese, M., Axås, J., Bäuerlein, B., Avila, K., Haller, G.: Data-driven modeling and prediction of non-linearizable dynamics via spectral submanifolds. Nat. Commun. **13**(1), 872 (2022). https://doi.org/10.1038/s41467-022-28518-y
53. Cenedese, M., Axås, J., Haocheng, Y., Eriten, M., Haller, G.: Data-driven nonlinear model reduction to spectral submanifolds in mechanical systems. Philos. Trans. Royal Soc. A: Math. Phys. Eng. Sci. **380**, 20210194 (2022). https://doi.org/10.1098/rsta.2021.0194
54. Axås, J., Cenedese, M., Haller, G.: Fast data-driven model reduction for nonlinear dynamical systems. Nonlinear Dyn. **111**, 7941–7957 (2023). https://doi.org/10.1007/s11071-022-08014-0
55. Cenedese, M., Marconi, J., Haller, G., Jain, S.: Data-assisted non-intrusive model reduction for forced nonlinear finite elements models. Nonlinear Dyn. (2024). https://doi.org/10.1007/s11071-024-10507-z
56. Kaszás, B., Cenedese, M., Haller, G.: Dynamics-based machine learning of transitions in Couette flow. Phys. Rev. Fluids **7**, L082402 (2022). https://doi.org/10.1103/PhysRevFluids.7.L082402
57. Xu, Z., Kaszás, B., Cenedese, M., Berti, G., Coletti, F., Haller, G.: Data-driven modelling of the regular and chaotic

dynamics of an inverted flag from experiments. J. Fluid Mech. **987**, R7 (2024). https://doi.org/10.1017/jfm.2024.411
58. Bettini, L., Cenedese, M., Haller, G.: Model reduction to spectral submanifolds in piecewise smooth dynamical systems. Int. J. Non-Linear Mech. **163**, 104753 (2024). https://doi.org/10.1016/j.ijnonlinmec.2024.104753
59. Alora, J., Cenedese, M., Schmerling, E., Haller, G., Pavone, M.: Data-driven spectral submanifold reduction for nonlinear optimal control of high-dimensional robots. In: 2023 IEEE International Conference on Robotics and Automation (ICRA), pp. 2627–2633 (2023). https://doi.org/10.1109/ICRA48891.2023.10160418
60. Yang, A., Axås, J., Kadár, F., Stépán, G., Haller, G.: Modeling nonlinear dynamics from videos. Nonlinear Dyn. **113**, 10881–10909 (2025). https://doi.org/10.1007/s11071-024-10687-8
61. Haller, G., Kaszás, B., Liu, A., Axås, J.: Nonlinear model reduction to fractional and mixed-mode spectral submanifolds. Chaos: Interdisciplin J Nonlin Sci **33**(6): 063138 (2023). https://doi.org/10.1063/5.0143936
62. Axås, J., Haller, G.: Model reduction for Nonlinearizable dynamics via delay-embedded spectral submanifolds. Nonlinear Dyn. **111**, 22079–22099 (2023). https://doi.org/10.1007/s11071-023-08705-2
63. Patko, D., Habib, G.: Dynamical integrity of periodic orbits: A computationally efficient approach. Nonlinear Dynamics (2025). https://doi.org/10.1007/s11071-025-11424-5
64. Jain, S., Tiso, P., Haller, G.: Exact nonlinear model reduction for a von Kármán beam: slow-fast decomposition and spectral submanifolds. J. Sound Vib. **423**, 195–211 (2018). https://doi.org/10.1016/j.jsv.2018.01.049
65. Jin, M., Chen, W., Brake, M.R., Song, H.: Identification of instantaneous frequency and damping from transient decay data. J. Vib. Acoust. **142**(5), 051111 (2020). https://doi.org/10.1115/1.4047416
66. Rega, G., Lenci, S., Ruzziconi, L.: Dynamical integrity: A novel paradigm for evaluating load carrying capacity. In: Global nonlinear dynamics for engineering design and system safety pp. 27–112 (2019). https://doi.org/10.1007/978-3-319-99710-0_2
67. Taylor, G.I.: An experimental study of standing waves. Proceedings of the Royal Society of London. Series A. Mathematical and Physical Sciences **218**(1132), 44–59 (1953). https://doi.org/10.1098/rspa.1953.0086
68. Ockendon, J., Ockendon, H.: Resonant surface waves. J. Fluid Mech. **59**(2), 397–413 (1973). https://doi.org/10.1017/S0022112073001618
69. Bäuerlein, B., Avila, K.: Phase lag predicts nonlinear response maxima in liquid-sloshing experiments. J. Fluid Mech. **925**, A22 (2021). https://doi.org/10.1017/jfm.2021.576
70. Peeters, M., Kerschen, G., Golinval, J.C.: Dynamic testing of nonlinear vibrating structures using nonlinear normal modes. J. Sound Vib. **330**(3), 486–509 (2011). https://doi.org/10.1016/j.jsv.2010.08.028
71. Takens, F.: Detecting strange attractors in turbulence, p. 366–381. Springer Berlin Heidelberg (1981). https://doi.org/10.1007/BFb0091924
72. Landau, L.D.: On the problem of turbulence. In: Dokl. Akad. Nauk USSR, vol. 44, p. 311 (1944)
73. Stuart, J.T.: On the non-linear mechanics of wave disturbances in stable and unstable parallel flows part 1. the basic behaviour in plane poiseuille flow. J. Fluid Mech. **9**(3), 353–370 (1960). https://doi.org/10.1017/S002211206000116X
74. Fujimura, K.: Centre manifold reduction and the stuart-landau equation for fluid motions. Proceedings of the Royal Society of London. Series A: Mathematical, Physical and Engineering Sciences **453**(1956), 181–203 (1997). https://doi.org/10.1098/rspa.1997.0011
75. Waite, J., Virgin, L.N., Wiebe, R.: Competing responses in a discrete mechanical system. Int. J. Bifurcation Chaos **24**(01), 1430003 (2014). https://doi.org/10.1142/S0218127414300031
76. Dowell, E.H.: A Modern Course in Aeroelasticity. Springer Nature, Cham (2022)
77. Lee, Y.S., Vakakis, A.F., Bergman, L.A., McFarland, D.M., Kerschen, G.: Suppression aeroelastic instability using broadband passive targeted energy transfers, part 1: Theory. AIAA J. **45**(3), 693–711 (2007). https://doi.org/10.2514/1.24062
78. Pettit, C.L., Beran, P.S.: Effects of parametric uncertainty on airfoil limit cycle oscillation. J. Aircr. **40**(5), 1004–1006 (2003). https://doi.org/10.2514/2.6889
79. Habib, G., Horváth, A.: Fold bifurcation identification through scientific machine learning. Phys. D **472**, 134490 (2025). https://doi.org/10.1016/j.physd.2024.134490
80. Liu, A., Axås, J., Haller, G.: Data-driven modeling and forecasting of chaotic dynamics on inertial manifolds constructed as spectral submanifolds. Chaos: Interdisciplin J Nonlin Sci (2024). https://doi.org/10.1063/5.0179741
81. Kovacic, I., Brennan, M.J.: The Duffing equation: nonlinear oscillators and their behaviour. John Wiley & Sons (2011)
82. Orlando, D., Gonçalves, P.B., Rega, G., Lenci, S.: Influence of transient escape and added load noise on the dynamic integrity of Multistable systems. Int. J. Non-Linear Mech. **109**, 140–154 (2019). https://doi.org/10.1016/j.ijnonlinmec.2018.12.001
83. Morsy, A.A., Xu, Z., Tiso, P., Haller, G.: Data-driven reduction of the finite-element model of a tribomechadynamics benchmark problem (2024). https://arxiv.org/abs/2409.05012
84. Bettini, L., Kaszás, B., Zybach, B., Dual, J., Haller, G.: Data-driven nonlinear model reduction to spectral submanifolds via oblique projection. Chaos: Interdisciplin J Nonlin Sci **35**(4) (2025). https://doi.org/10.1063/5.0243849
85. Mazzilli, N.C.E., Guilherme, R.F.: Structural reliability analysis of a stable equilibrium point based on the dynamic integrity of its safe basin. Nonlinear Dyn. (2024). https://doi.org/10.1007/s11071-024-10777-7